Article

SOURCE DATA TRANSPARENT PROCESS

EMBO reports

A genome-wide association study identifies a transporter for zinc uploading to maize kernels

Zhen-Fei Chao[1,2,†], Yuan-Yuan Chen[3,†], Chen Ji[1,2,†], Ya-Ling Wang[1], Xing Huang[1,2], Chu-Ying Zhang[1,4], Jun Yang[5], Tao Song[1,2], Jia-Chen Wu[1,2], Liang-Xing Guo[1,2], Chu-Bin Liu[1,2], Mei-Ling Han[1], Yong-Rui Wu[1], Jianbing Yan[3] & Dai-Yin Chao[1,*]

Abstract

The Zn content in cereal seeds is an important trait for crop production as well as for human health. However, little is known about how Zn is loaded to plant seeds. Here, through a genome-wide association study (GWAS), we identify the Zn-NA (nicotianamine) transporter gene *ZmYSL2* that is responsible for loading Zn to maize kernels. High promoter sequence variation in *ZmYSL2* most likely drives the natural variation in Zn concentrations in maize kernels. ZmYSL2 is specifically localized on the plasma membrane facing the maternal tissue of the basal endosperm transfer cell layer (BETL) and functions in loading Zn-NA into the BETL. Overexpression of *ZmYSL2* increases the Zn concentration in the kernels by 31.6%, which achieves the goal of Zn biofortification of maize. These findings resolve the mystery underlying the loading of Zn into plant seeds, providing an efficient strategy for breeding or engineering maize varieties with enriched Zn nutrition.

Keywords biofortification; genome-wide association study; maize kernel; YSL2; zinc

Subject Category Plant Biology

DOI 10.15252/embr.202255542 | Received 6 June 2022 | Revised 9 October 2022 | Accepted 17 October 2022

EMBO Reports (2022) e55542

Introduction

Zn biofortification of cereal-based food is a fundamental method to address the problem of Zn deficiency, which affects 17% of people worldwide, and genetic improvement of the Zn content in cereal grains is the most economical and effective measure (White & Broadley, 2009; Maqbool & Beshir, 2019). Maize is one of the most important food crops in the world and one of the leading edible crops in regions with Zn malnutrition (Maqbool & Beshir, 2019; Gashu *et al*, 2021). However, maize typically has the lowest Zn concentration of all cereal crops, people relying on maize-based diets are therefore most likely to suffer from Zn deficiency (Gashu *et al*, 2021). The large variation in kernel Zn content has been found (Long *et al*, 2004) to be largely due to genetic contributions (Simic *et al*, 2012; Baxter *et al*, 2013), suggesting that genetic improvement of Zn biofortification in maize is feasible. However, no genetic locus controlling natural variation in the Zn content of maize kernels has been successfully cloned, limiting genetic strategies for Zn biofortification.

Based on studies conducted mainly in *Arabidopsis thaliana*, a series of genes controlling the uptake and long-distance transport of Zn have been identified and characterized. Zn uptake from the rhizosphere is controlled by metal-ion transporters of the ZRT- and IRT-like protein (ZIP) family (Robinson *et al*, 1999; Vert *et al*, 2002), while heavy metal-transporting P1B-ATPases (HMAs) 2 and 4 are responsible for the long-distance transport of Zn from roots to shoots (Hussain *et al*, 2004; Hanikenne *et al*, 2008). Yellow stripe 1 (YS1) and YS1-like (YSL) proteins function in transporting metals complexed with phytosiderophores or nicotianamine (NA) into the cell and have been extensively studied for their roles in root uptake and phloem loading of Fe (Curie *et al*, 2001; Le Jean *et al*, 2005). However, there is conflicting evidence on the role of YSL transporters in Zn homeostasis (Waters & Grusak, 2008), questioning whether and how YSL transporters control Zn homeostasis.

The transport of Zn from the mother plant to seeds is critical for biofortification. This process involves at least two steps: unloading of Zn from the mother plant to the maternal–filial interface and uploading of Zn from the maternal–filial interface to the seed domain. In *A. thaliana*, HMA2 and HMA4 were found to mediate the export of Zn from maternal tissues to the apoplastic space between the seed and the mother plant (Olsen *et al*, 2016). Their ortholog in barley, HvHMA4, was also found to be expressed in the cells connecting the maternal domain and the filial tissue (Tauris

1 National Key Laboratory of Plant Molecular Genetics, CAS Center for Excellence in Molecular Plant Sciences, Shanghai Institute of Plant Physiology and Ecology, Chinese Academy of Sciences, Shanghai, China
2 University of Chinese Academy of Sciences, Beijing, China
3 National Key Laboratory of Crop Genetic Improvement, Huazhong Agricultural University, Wuhan, China
4 School of Life Science, Henan University, Kaifeng, China
5 National Engineering Laboratory of Crop Stress Resistance, School of Life Science, Anhui Agricultural University, Hefei, China
*Corresponding author. Tel: +86 21 54924358; E-mail: dychao@cemps.ac.cn
†These authors contributed equally to this work

et al, 2009), suggesting that a similar mechanism of uploading of Zn from the mother plant exists in barley. However, it is unknown how Zn is loaded to filial tissues from the maternal–filial interface.

ZmYSL2 was reported to function as metal–NA transporter to control endosperm development by affecting Fe distribution between the embryo and the endosperm (Zang *et al*, 2020; He *et al*, 2021). However, there were conflicting results about whether *ZmYSL2* affects the total Fe content of the kernels (Zang *et al*, 2020; He *et al*, 2021). Besides, the reported expression pattern of *ZmYSL2* in aleurone and sub-aleurone layers in endosperm seemed inconsistent with the ion phenotype of the mutants (He *et al*, 2021), questioning the functional mechanisms of *ZmYSL2*. In addition, Fe^{3+}-DMA was found to be the major form of Fe in the phloem of cereal plants (Nishiyama *et al*, 2012), and DMA but not NA affects the delivery of Fe into the seeds of gramineous plants (Diaz-Benito *et al*, 2018; Chao & Chao, 2022). Instead, Zn-NA is the major form of Zn in cereal phloem and NA but not DMA controls the translocation of Zn into the gramineous seeds (Nishiyama *et al*, 2012; Diaz-Benito *et al*, 2018). These data suggested that the role of *ZmYSL2* in metal homeostasis needs to be addressed.

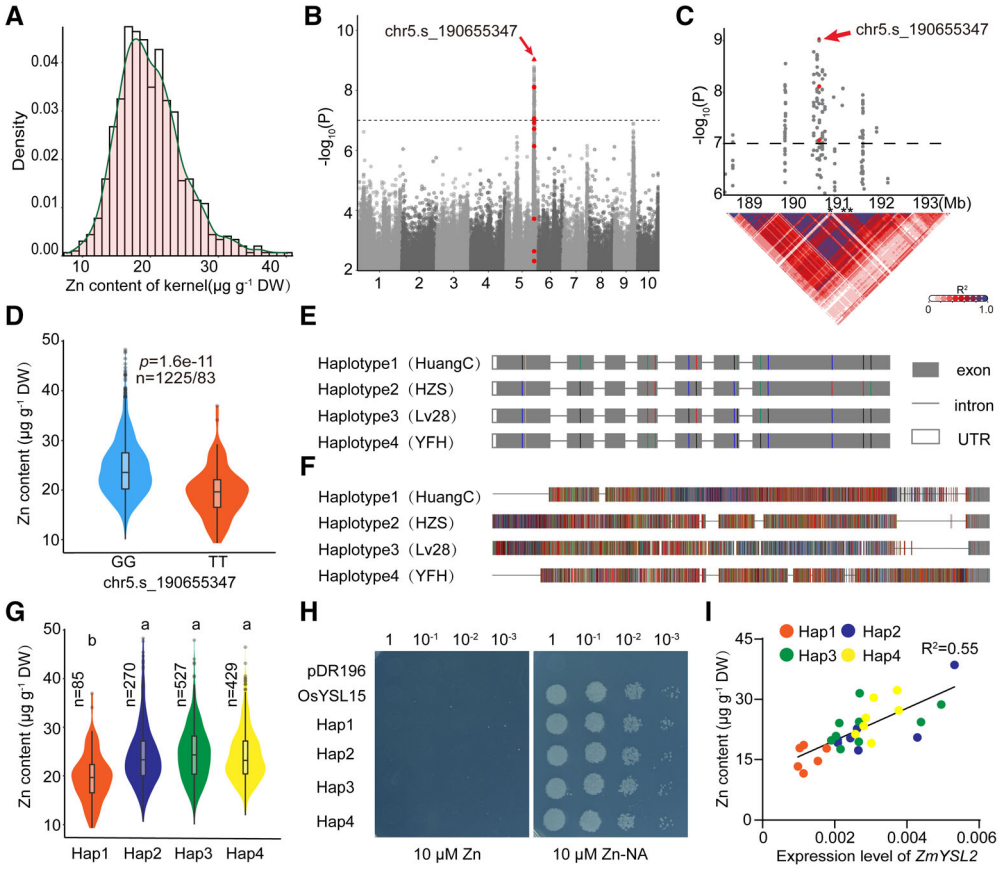

Figure 1. GWAS for the kernel Zn content in maize.

A Frequency distribution of the seed Zn concentration in 1311 progenies of the CUBIC population.

B Manhattan plot for the GWAS. The dashed horizontal line depicts the Bonferroni-adjusted significance threshold ($P = 1.0 \times 10^{-7}$). The SNPs located within the candidate genes are labeled as red dots. The red arrow indicates the most significant SNP chr5.s_190655347.

C Regional Manhattan plot of the candidate genomic region on chromosome 5 and pairwise LD analysis. The 2-Mb genomic region on either side of the most significant SNP is shown. The SNPs located within the candidate genes are labeled as red dots. The red arrow indicates the most significant SNP.

D Zn content of the genotypes of the CUBIC population separated by the peak SNP. *n* denotes the number of genotypes. The central band in the boxplot represents the median of the sample values and the boxes depict the interquartile range. The whiskers indicate variability outside the upper and lower quartiles.

E, F Haplotypes (Hap) of the *ZmYSL2* gene body (**E**) and promoter (5 kb before ATG) (**F**) region among maize natural variations. SNPs in each haplotype are indicated in different colors, where red indicates T, black indicates G, blue indicates C, and green indicates A. Gray indicates the same sequences among each haplotype.

G Zn content of four haplotypes. *n* denotes the number of genotypes belonging to each haplotype group. Statistical significance was determined by ANOVA. The different lowercase letters above the bars indicate significant differences by one-way ANOVA ($P < 0.01$). The central band in the boxplot represents the median of the sample values and the boxes depict the interquartile range. The whiskers indicate variability outside the upper and lower quartiles.

H Substrate transport activity test of four haplotypes. The *zrt1zrt2* mutant yeast strain was transformed with different vectors. Yeast cells were spotted on SD-Ura medium containing $ZnSO_4$ (10 μM) or Zn-NA (10 μM). Plates were incubated for 3 days at 30°C.

I Correlation analysis of the Zn content in mature maize seeds and *ZmYSL2* expression level at 20 DAP. Each haplotype was labeled with different colors as indicated.

Source data are available online for this figure.

In this study, we performed a genome-wide association study (GWAS) to identify a QTL controlling natural variation in the kernel Zn content. We established that the YSL family transporter *ZmYSL2* is the causal gene in the kernel Zn QTL, which is specifically expressed in the maize basal endosperm transfer layer (BETL) and functions in the uploading Zn-NA into the filial domain from the maternal–filial interface. Overexpression of *ZmYSL2* was able to significantly increase the Zn concentration by 30%. This study not only is the first to clone a QTL controlling the kernel Zn content of maize and identified a transporter for zinc uploading to maize kernels but also offers a new method for breeding Zn-biofortified crops.

Results

GWAS of Zn content in maize kernels

We analyzed the kernel Zn concentrations of 1,404 inbred lines from a synthetic, complete-diallel design plus an unbalanced breeding-like inter-cross (CUBIC) population (Liu *et al*, 2020b) and observed kernel Zn concentrations ranging from 9.2 to 48.3 μg g^{-1} dry weight (DW) across the population (Fig 1A). We performed a GWAS by applying a mixed-model approach to reveal a 300 kb interval on chromosome 2 containing 85 SNPs that were closely associated with variation in the kernel Zn content (P-values < 10^{-7}) (Fig 1B and C). The most closely associated SNP (−log P-value = 9.03) is Chr5_190655347 (B73 v3). The lines with two guanines (GG) at Chr5_190655347 had average kernel Zn concentrations 22.8% higher than those of the lines with two thymines (TT), and the minor T allele was present in 6.7% of the lines studied (Fig 1D).

Of the 10 genes localized in the 300 kb LD region of the top SNP (Table 1), GRMZM2G135291 and GRMZM2G156599 encoded two proteins belonging to the YSL family, namely *ZmYSL2* and *ZmYS1*, which could be the best candidates for controlling the natural variation in the kernel Zn concentrations of maize. However, *ZmYS1* has been reported to control iron (Fe) uptake from the soil, and loss of function of *ZmYS1* results in a severe shoot deficiency phenotype (Curie *et al*, 2001), but we did not identify any SNPs around this locus that were significantly associated with the leaf or kernel Fe concentrations (Fig EV1A–F), suggesting that there was no functional variation present in *ZmYS1* and that *ZmYSL2* may thus be responsible for the natural variation in the kernel Zn concentrations of maize.

We analyzed the *ZmYSL2* sequences of the 24 parents used to generate the CUBIC population and found numerous polymorphic sites present in the *ZmYSL2* genomic region (Fig 1E), which can be divided into four major haplotypes (Table 2), with haplotype I accumulating 18.6% less Zn in the kernels than the other three haplotypes (Fig 1G). The four *ZmYSL2* haplotypes encoded four different ZmYSL2 protein variants, but all the amino acid variations in four haplotypes were non-conserved sites among YSL2 orthologs (Appendix Fig S1) and all these *ZmYSL2* variants were able to complement the Zn-uptake defective yeast mutant *zrt1zrt2* when the growth medium was supplemented with 10 μM Zn-NA but not when the growth medium was supplemented with 10 μM Zn (Fig 1H). These data supported that *ZmYSL2* functions in uploading Zn-NA to the kernel, but the amino acid changes among these variants are not responsible for natural variation in the kernel Zn concentrations.

In contrast to the gene body region, the promoter region of *ZmYSL2* exhibited much greater variability. Except for the 300-bp region upstream of the start codon of *ZmYSL2*, the 5-kb promoter regions shared little similarity (Fig 1F). The expression of *ZmYSL2* in the kernels was linearly positively correlated with the kernel Zn concentration (Fig 1I) but not with the kernel Fe concentrations (Fig EV1G). In addition, the lines with haplotype I showed significantly lower *ZmYSL2* expression in kernels than the lines with the other three haplotypes (Fig 1I). In contrast, there is no polymorphism in the intron region significantly associated with the variation in the kernel Zn concentration (Appendix Fig S2). These data indicated that polymorphisms in the promoter of *ZmYSL2* most likely drive natural variations in the expression of *ZmYSL2* and the kernel Zn concentrations.

ZmYSL2 controls total Zn but not Fe content in the kernels

To further study the role of *ZmYSL2*, we isolated four genetic mutants for this gene (Figs 2A–G and EV2). Among them, *criysl2-1*

Table 1. Genes within 300 kb of the SNP most closely associated with the kernel content Zn in the CUBIC population.

Gene_ID	Start	Stop	Annotation	Ortholog in *A. thaliana*	Distance to peak SNP
GRMZM2G117164	190526952	190528628	Homeobox leucine zipper protein ATHB-6	AT3G61890	126,719 bp
GRMZM2G117238	190532564	190536335	Origin recognition complex subunit 2	AT2G37560	119,012 bp
GRMZM2G072865	190605603	190612676	ATP-dependent zinc metalloprotease FTSH7	AT3G47060	42,671 bp
GRMZM2G135385	190614417	190615314	Cytochrome b5	AT2G46650	40,033 bp
GRMZM2G135291	**190656253**	**190659274**	**Iron-nicotianamine transporter yellow stripe like 2**	**AT5G53550**	**906 bp**
GRMZM2G156599	**190726051**	**190729182**	**Iron–phytosiderophore transporter yellow stripe 1**	**AT5G53550**	**70,703 bp**
GRMZM2G156585	190735441	190737796	Threonine synthase 1	AT4G29840	80,094 bp
GRMZM2G156575	190738088	190739754	Unknown protein	AT5G51170	82,741 bp
GRMZM6G037947	190741052	190741387	Unknown protein	–	85,705 bp
GRMZM2G031952	190786926	190791823	ELMO domain-containing protein 2	AT3G60260	131,579 bp

Table 2. Nucleotide and amino acid variations in exons of *ZmYSL2* among four haplotypes.

Nucleotide acid position (reference to B73)								
Haplotype	**Maize cultivar**	**196**	**209**	**705**	**1201**	**1291**	**1495**	**1540**
Hap1	HuangC	G	AGC	A	A	T	C	T
	E28	G	AGC	A	A	T	C	T
	B73	G	AGC	A	A	T	C	T
Hap2	HZS	C	AGC	G	T	T	C	G
	HYS	C	AGC	G	T	T	C	G
	NX110	C	AGC	G	T	T	C	G
	Chang7-2	C	AGC	G	T	T	C	G
	Lx9801	C	AGC	G	T	T	C	G
	Ji853	C	AGC	G	T	T	C	G
	W22	C	AGC	G	T	T	C	G
	W64A	C	AGC	G	T	T	C	G
Hap3	Lv28	C	–	G	T	T	G	T
	Ji53	C	–	G	T	T	G	T
	K12	C	–	G	A	T	G	T
	Shuang741	C	–	G	T	T	G	T
	Zong31	C	AGCAGC	G	A	T	G	T
	F349	C	AGCAGC	G	A	T	C	G
	Zi330	C	AGCAGC	G	A	T	G	T
Hap4	YFH	C	AGCAGC	G	A	A	C	G
	Xi502	C	AGCAGC	G	A	A	C	G
	Q1261	C	AGCAGC	G	A	A	C	G
	TY4	C	AGCAGC	G	A	A	C	G
	Dan340	C	AGCAGC	G	A	A	C	G
	H21	C	AGCAGC	G	A	A	C	G
	Zong3	C	–	G	A	A	C	G
	81,515	C	AGCAGC	G	A	A	C	G
	5,237	C	AGCAGC	G	A	A	C	G
	KN5585	C	AGCAGC	G	A	A	C	G
Amino acid change and location (reference to B73)		**V66L**	**Q**	**N179D**	**I261F**	**W291R**	**L324V**	**Y339D**

Nucleotide acid position (reference to B73 genome)								
Haplotype	**Maize cultivar**	**1814**	**1816**	**1943**	**2016**	**2522**	**2725**	**2729**
Hap1	HuangC	G	A	A	C	C	G	G
	E28	G	A	A	C	C	G	G
	B73	G	A	A	C	C	G	G
Hap2	HZS	C	A	A	C	T	T	A
	HYS	C	A	A	C	T	T	A
	NX110	C	A	A	C	T	T	A
	Chang7-2	C	A	A	C	T	T	A
	Lx9801	C	A	A	C	T	T	A
	Ji853	C	A	A	C	T	T	A

Table 2 (continued)

Nucleotide acid position (reference to B73 genome)								
Haplotype	**Maize cultivar**	**1814**	**1816**	**1943**	**2016**	**2522**	**2725**	**2729**
	W22	C	A	A	C	T	T	A
	W64A	C	A	A	C	T	T	A
Hap3	Lv28	C	G	A	G	C	G	G
	Ji53	C	G	A	G	T	T	A
	K12	C	G	A	G	T	G	G
	Shuang741	C	G	A	G	C	G	G
	Zong31	C	G	A	G	T	G	G
	F349	C	A	A	C	T	T	A
	Zi330	C	G	A	G	T	T	A
Hap4	YFH	C	G	G	C	C	G	G
	Xi502	C	G	G	C	C	G	G
	Q1261	C	G	G	C	C	G	G
	TY4	C	G	G	C	C	G	G
	Dan340	C	G	G	C	C	G	G
	H21	C	G	G	C	C	G	G
	Zong3	C	G	A	G	T	G	G
	81,515	C	G	G	C	C	G	G
	5,237	C	G	G	C	C	G	G
	KN5585	C	G	G	C	C	G	G
Amino acid change and position (reference to B73)		**S399T**	**S400G**	**I411V**	**A435G**	**P604S**	**L671F**	**V673M**

Reference B73, three wild-type background W22, W64A, KN5585, and 24 parents of the CUBIC population were shown and all the materials were classified into four haplotypes according to sequence similarity. Numbers in the first row show the positions of nucleotide acid variation which causes sense amino acid variations on the gene body of *ZmYSL2* in reference B73 starting from the start codon ATG. The last row shows the amino acid changes and positions on the protein of *ZmYSL2* in reference B73 starting from the first amino acid Met.

and *criysl2-2* were knockout mutants generated by CRISPR-Cas9 technology in the KN5585 background (Figs 2B and C and EV2B). The mutant *zmysl2-1* was a transposon-insertion mutant in the W22 background (Figs 2D and EV2A). The mutant *zmysl2-2* was an EMS-mutagenized mutant in the W64A background (Figs 2E–G and EV2C), in which the conserved alanine at the 133rd residue was substituted with a valine (Fig EV2C).

By using a micro-X-ray fluorescence spectrometer (μXRF), we observed that Zn was enriched in the embryos of the kernels, and the Zn content in the kernels carrying a homozygous knockout or impaired allele of *ZmYSL2* was notably lower than that in the corresponding wild-type kernels from the same self-pollinated heterozygous ear (Fig 2H–J; i.e., kernels carrying homozygous *criysl2-1* accumulated much less Zn than wild-type kernels from the same ear). This observation was further confirmed by elemental analysis by inductively coupled plasma-mass spectrometry (ICP-MS), which showed that the kernels carrying homozygous mutant alleles of *ZmYSL2* accumulated much less Zn in either the embryos or endosperm than the kernels with the corresponding wild-type genotypes from the same ear (Fig 2K–S). These data showed that loading Zn to the kernels requires *ZmYSL2*; specifically, it requires *ZmYSL2* expressed in the filial tissues of the kernels.

Compared with the Zn content, the total Fe content in the kernels was not affected by mutation of *ZmYSL2* (Fig EV3A, D, and G). However, the Fe distribution was changed in the kernels of *crisysl2-1*, *crisysl2-2*, and *zmysl2-1*, in which Fe was accumulated in the endosperm rather than embryo (Fig EV3B, C, E, F, and H–L), indicating that the mother-to-offspring delivery mechanism of Fe is different from that of Zn and *ZmYSL2* may control Fe transport from endosperm to embryo in an unknown manner. As ZmYSL2 can transport Fe(II)-NA (Fig EV3M) (Zang *et al*, 2020; He *et al*, 2021), we wondered whether Fe is transported into the filial tissue of maize in another form that is not a substrate of ZmYSL2. Previous studies reported that Fe(III)-DMA is the major Fe form in the phloem of gramineous plants (Nishiyama *et al*, 2012) and DMA rather than NA is essential for Fe accumulation in cereal seeds (Diaz-Benito *et al*, 2018), indicating that Fe(III)-DMA rather than Fe(II)-NA is the major form for Fe transport into the maize kernel. We then confirmed that Fe(III)-DMA is not a substrate of ZmYSL2 by using yeast complementation experiment (Fig EV3M), explaining why mutation of ZmYSL2 does not affect the total Fe content in the kernels. Phytic acid is another Fe chelator in seeds and its content was not changed in the kernels of *zmysl2-1* (Appendix Fig S3).

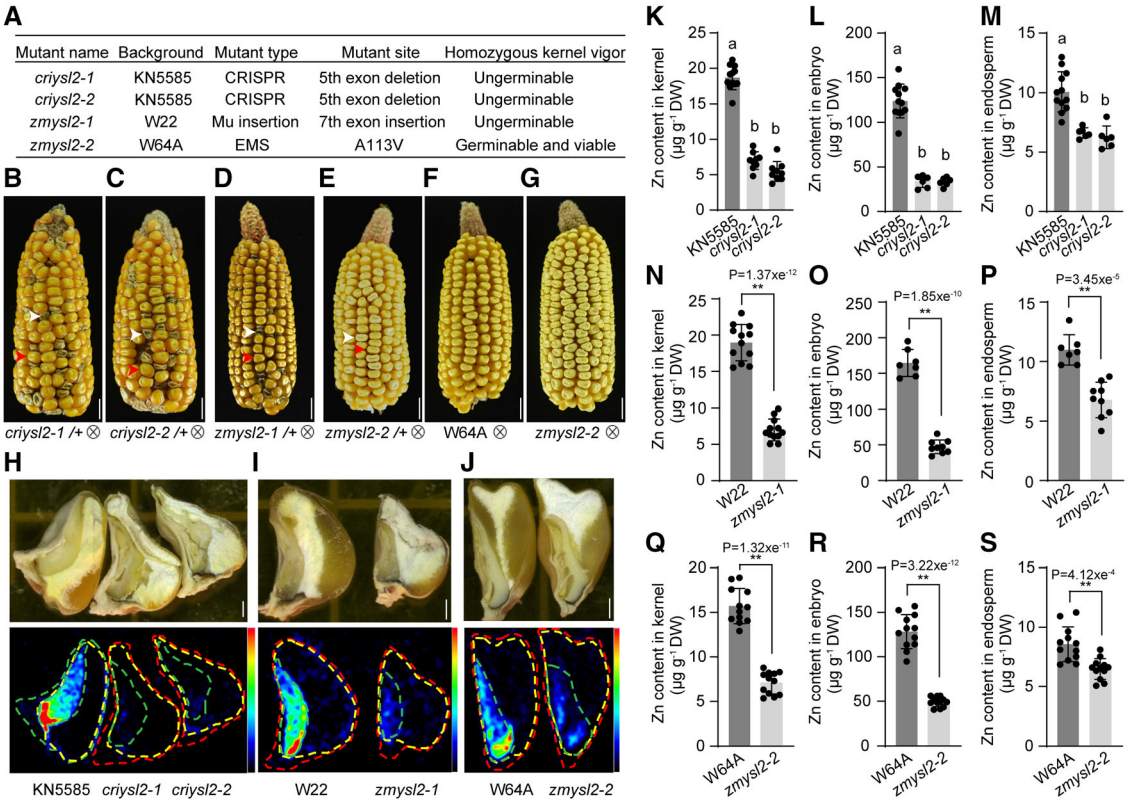

Figure 2. *ZmYSL2* is responsible for loading Zn into maize kernels.

A Information for the *ZmYSL2* mutants.

B–G Representative ear images of heterozygous *criysl2-1* (B), *criysl2-2* (C), *zmysl2-1* (D), and *zmysl2-2* (E) plants and homozygous *zmysl2-2* (G) and the corresponding wild-type W64A (F) plants. The white arrow indicates genotyped homozygous *criysl2-1*, *criysl2-2*, *zmysl2-1*, and *zmysl2-2* seeds and the red arrow indicates corresponding genotyped wild type. Scale bars, 1 cm.

H–J μXRF analysis of the Zn content and distribution in kernels of homozygous *criysl2-1* (H), *criysl2-2* (H), *zmysl2-1* (I), and *zmysl2-2* (J) mutants and the corresponding wild-type genotypes. The upper panel shows the mature kernels cut in half, and the lower panel shows the Zn content and distribution. The dashed line depicts different parts of the kernel, where the red line indicates the whole kernel, the yellow line indicates the embryo and endosperm, and the green line indicates the embryo.

K–S Zn content in whole kernels (K, N, Q), embryos (L, O, R), and endosperm (M, P, S) of *criysl2-1/2* (K–M), *zmysl2-1* (N–P), and *zmysl2-2* (Q–S) detected by ICP-MS. Samples of mature kernels were collected. The data represent the means ± SDs. $n = 6$–12 biological replicates. Statistical significance was determined by ANOVA in (K–M) and Student's *t*-test in (N–S). The different lowercase letters above the bars indicate significant differences by one-way ANOVA ($P < 0.01$) (K–M). $^{**}P < 0.001$ (Student's *t*-test).

The opaque phenotype of *ZmYSL2* mutants is due to deficiency of Zn in the kernels

In addition to the ion phenotype, we found that the kernels in homozygous *criysl2-1*, *criysl2-2*, or *zmysl2-1* genotypes derived from the self-pollinated heterozygous knockout mutants showed an opaque endosperm and were not able to germinate (Fig 2A–G), which is consistent with previous reports (Zang *et al*, 2020; He *et al*, 2021). In contrast, although the kernels in homozygous *zmysl2-2* also showed an opaque phenotype (Fig 2A and G), they were germinable and viable, suggesting that *zmysl2-2* was a weak allele. Moreover, the Zn concentrations in the kernels of *crisysl2-1*, *crisysl2-2*, and *zmysl2-1* were decreased 73.0%–71.3% compared with those in the corresponding wild types, while *zmysl2-2* accumulated Zn in the kernels 62.7% less than wild-type W64A (Fig 2K, N, and Q). This result further indicated that *zmysl2-2* was a weak allele rather than a knockout allele. *ZmYSL2* was recently reported to control endosperm development by affecting the distribution of Fe between the embryo and the endosperm (Zang *et al*, 2020). Considering that the Fe distribution was not affected in *zmysl2-2* and kernels of *zmysl2-2* were opaque and viable, these data suggested that the opaque phenotype was caused by Zn deficiency, while the embryo lethal phenotype was caused by Fe deficiency, which is consistent with our previous observation in *A. thaliana* (Chao *et al*, 2021). Kernels carrying homozygous mutant alleles of *ZmYSL2* also accumulated much less cobalt (Co) than the kernels with the corresponding wild-type genotypes from the same ear (Tables 3–4), indicating that loading Co to the kernels also requires *ZmYSL2*. These data are also consistent with our finding in *A. thaliana*, which revealed that translocation of Co to seed is dependent on NA but lack of Co does affect seed development (Chao *et al*, 2021).

Table 3. Kernel element profile of *crizmysl2* mutants and the corresponding wild-type.

Element	Content (μg/g DW)			Percentage difference from KN5585 (%)		*P*-values
	KN5585	*criysl2-1*	*criysl2-2*	*criysl2-1*	*criysl2-2*	
B	103.55 ± 7.98	101.26 ± 15.96	106.38 ± 16.47	−2.22	2.73	ns
Na	0.15 ± 0.04	0.14 ± 0.04	0.16 ± 0.04	−6.95	9.57	ns
Mg	473.74 ± 43.98	500.19 ± 76.00	455.10 ± 86.59	5.58	−3.93	ns
P	2800.65 ± 412.75	2625.68 ± 316.05	3097.46 ± 360.83	−6.25	10.60	ns
S	577.48 ± 61.40	531.61 ± 70.60	566.38 ± 49.11	−7.94	−1.92	ns
K	4630.48 ± 513.13	4684.84 ± 706.40	4549.11 ± 580.89	1.17	−1.76	ns
Ca	328.06 ± 60.76	343.51 ± 67.09	276.79 ± 79.57	4.71	−15.63	ns
Ti	7.42 ± 0.73	8.60 ± 1.86	7.86 ± 1.91	16.01	5.94	ns
Cr	0.07 ± 0.02	0.07 ± 0.01	0.07 ± 0.03	5.41	14.86	ns
Mn	9.80 ± 1.89	9.97 ± 1.83	10.31 ± 1.61	1.80	5.18	ns
Fe	17.32 ± 1.71	18.58 ± 2.85	16.92 ± 2.08	7.25	−2.31	ns
Co	**0.0044 ± 0.0007**	**0.0021 ± 0.0006**	**0.0020 ± 0.0007**	**−53.07**	**−53.96**	**< 0.0006**
Ni	0.12 ± 0.04	0.11 ± 0.55	0.12 ± 0.03	−7.89	−2.91	ns
Cu	1.10 ± 0.09	1.10 ± 0.16	1.20 ± 0.26	0.03	8.43	ns
Zn	**18.70 ± 1.67**	**6.99 ± 1.24**	**5.46 ± 1.41**	**−62.61**	**−70.82**	**< 0.0006**
As	0.04 ± 0.01	0.05 ± 0.02	0.04 ± 0.01	22.01	−4.76	ns
Se	1.24 ± 0.43	1.58 ± 0.40	1.32 ± 0.33	27.33	6.28	ns
Rb	1.58 ± 0.19	1.47 ± 0.40	1.42 ± 0.50	−6.95	−10.13	ns
Sr	0.64 ± 0.13	0.68 ± 0.19	0.51 ± 0.18	6.22	−19.31	ns
Mo	0.03 ± 0.003	0.02 ± 0.004	0.02 ± 0.005	−10.12	−5.31	ns
Cd	0.009 ± 0.003	0.009 ± 0.002	0.009 ± 0.003	−0.71	−9.52	ns
Pb	0.64 ± 0.14	0.61 ± 0.13	0.58 ± 0.15	−4.55	−8.98	ns

Data represent the mean ± SD (n = 9–12). Data in bold represent elements with a significant difference ($P \leq 0.01$) between the *crizmysl2* mutants and KN5585 in both mutants. ns, not significant. Statistical significance was determined by Student's *t*-test. Source data are available online for this Table.

Allelism tests for different *ZmYSL2* mutants

To confirm that the phenotypes above were caused by mutation of *ZmYSL2*, we performed pairwise crosses among *criysl2-1*/+, *zmysl2-1*/+, and homozygous *zmysl2-2* (Fig 3). We found that the low Zn kernels and high Zn kernels on the ears from the crosses between *zmysl2-1*/+ and *criysl2-1*/+ segregated in a 1:3 segregation ratio (Fig 3A and B and Table 5) as expected and the low Zn phenotype and the opaque phenotype were co-segregated. In addition, all the kernels with low Zn content and opaque phenotype bear a *criysl2-1/zmysl2-1* genotype, indicating that those phenotypes of *criysl2-1* and *zmysl2-1* are caused by the same gene (Fig 3B and C and Table 5).

Consistent with the above observation, the segregation ratio of the low Zn kernels and high Zn kernels on the ears from the crosses between *zmysl2-1*/+ and *zmysl2-2* was 1:1 (Fig 3A and B and Table 5) and the opaque phenotype was also co-segregated with the low Zn phenotype. Moreover, all the kernels with a *zmysl2-1/zmysl2-2* genotype showed opaque endosperm and low Zn phenotype (Fig 3B and C and Table 5). These data confirmed that *zmysl2-1* and *zmysl2-2* are two loss-of-function/reduced alleles of the same locus. The crosses between *criysl2-1*/+ and *zmysl2-2* confirmed that *criysl2-1* and *zmysl2-2* are two alleles of the same gene. These data together established that *ZmYSL2* is the causal gene responsible for the low Zn and opaque phenotypes of the three mutants.

Furthermore, the pairwise crossed ears with *criysl2-1*, *zmysl2-1*, and *zmysl2-2* genotypes all exhibited low-Zn phenotypes while abnormal Fe distribution phenotype was only observed in kernels with *zmysl2-1/criysl2-1* and *criysl2-1/zmysl2-1* genotype (Fig 3D). These data further supported that the opaque phenotype was caused by Zn deficiency.

ZmYSL2 is responsible for loading Zn from the placenta–chalaza domain to the BETL

According to the qRT–PCR results, *ZmYSL2* was predominantly expressed in kernels after 12 days after pollination (DAP) (Fig 4A). Further investigation showed that *ZmYSL2* was dramatically upregulated in the endosperm beginning at 12 DAP but not in the embryo or the endosperm without BETL tissue (Fig 4B). These data suggested that *ZmYSL2* is predominantly expressed in the BETL during the filling stage, which was then confirmed by *in situ* hybridization of *ZmYSL2* (Fig 4C). Expression of ZmYSL2-GFP in protoplasts isolated from leaf of *A. thaliana* showed that ZmYSL2-GFP is localized

Table 4. Kernel element profile of *zmysl2-1*, *zmysl2-2*, and the corresponding wild type.

Element	Content (μg g DW^{-1})				Percentage difference from WT (%)		*P*-values
	W22	*zmysl2-1*	W64A	*zmysl2-2*	*zmysl2-1*	*zmysl2-2*	
B	75.86 ± 16.87	81.12 ± 21.79	90.15 ± 17.58	97.97 ± 12.99	6.94	8.68	ns
Na	0.10 ± 0.03	0.12 ± 0.03	0.12 ± 0.01	0.12 ± 0.03	13.59	0.07	ns
Mg	415.61 ± 46.61	401.31 ± 74.60	586.57 ± 49.68	562.73 ± 52.29	−3.44	−4.06	ns
P	2879.30 ± 410.01	2565.63 ± 677.66	3618.49 ± 573.40	3501.93 ± 361.83	−10.89	−3.22	ns
S	392.11 ± 56.58	418.49 ± 93.96	568.28 ± 92.46	601.32 ± 52.79	6.73	5.81	ns
K	2702.49 ± 377.53	2516.47 ± 222.70	3527.67 ± 577.60	3743.58 ± 604.17	−6.88	6.12	ns
Ca	129.24 ± 44.38	144.26 ± 34.32	156.26 ± 28.42	162.59 ± 38.01	11.62	4.03	ns
Ti	7.40 ± 1.17	7.97 ± 1.93	8.76 ± 1.25	8.46 ± 1.10	7.65	−3.35	ns
Cr	0.05 ± 0.01	0.05 ± 0.01	0.03 ± 0.01	0.04 ± 0.01	−4.83	16.54	ns
Mn	5.79 ± 0.77	5.28 ± 1.14	6.18 ± 0.70	6.66 ± 0.096	−8.80	7.89	ns
Fe	17.77 ± 2.63	17.95 ± 3.19	20.61 ± 2.42	20.01 ± 2.28	1.03	−2.91	ns
Co	**0.0053 ± 0.0005**	**0.0029 ± 0.0007**	**0.0138 ± 0.0015**	**0.0067 ± 0.0009**	**−45.63**	**−51.57**	**< 0.0006**
Ni	0.34 ± 0.11	0.35 ± 0.08	0.80 ± 0.84	0.61 ± 0.66	4.14	−23.01	ns
Cu	2.04 ± 0.31	1.50 ± 0.21	0.81 ± 0.14	0.85 ± 0.16	−26.71	4.89	ns
Zn	**18.96 ± 2.49**	**6.98 ± 1.50**	**15.71 ± 1.99**	**7.08 ± 1.25**	**−63.17**	**−54.91**	**< 0.0006**
As	0.05 ± 0.01	0.05 ± 0.01	0.06 ± 0.01	0.06 ± 0.01	5.91	1.02	ns
Se	1.39 ± 0.51	1.47 ± 0.59	0.86 ± 0.11	0.97 ± 0.20	5.85	13.78	ns
Rb	1.55 ± 0.21	1.59 ± 0.27	1.19 ± 0.19	1.17 ± 0.24	2.63	−2.04	ns
Sr	0.22 ± 0.06	0.24 ± 0.05	0.15 ± 0.05	0.15 ± 0.05	10.71	2.26	ns
Mo	0.05 ± 0.006	0.04 ± 0.009	0.02 ± 0.003	0.02 ± 0.002	−10.76	3.51	ns
Cd	0.008 ± 0.003	0.008 ± 0.002	0.007 ± 0.001	0.007 ± 0.001	−0.25	−6.40	ns
Pb	0.51 ± 0.12	0.51 ± 0.13	0.53 ± 0.10	0.47 ± 0.08	−1.34	−11.39	ns

Data represent the mean ± SD ($n = 12$). Data in bold represent elements with a significant difference ($P \leq 0.01$) between the mutants and wild type in both mutants. ns, not significant. Statistical significance was determined by Student's *t*-test. Source data are available online for this Table.

on plasma membrane (Fig 4D). An immunofluorescence assay using a specific ZmYSL2 antibody further indicated that ZmYSL2 was specifically localized on the plasma membrane of BETL cells facing the apoplastic space between the maternal tissue and the filial domain (Fig 4E). These data established that *ZmYSL2* functions in the uptake of Zn-NA from the maternal–filial interface to the BETL, a zone for transferring nutrients from the maternal tissue to the filial domain.

Perfectly matching the expression pattern of *ZmYSL2*, the Zn concentrations in the wild-type kernels gradually increased from 12 DAP (Fig 5A–C), while the Zn concentrations in the mutant kernels did not change until the late filling stage (Fig 5A–C). These results were further confirmed by μXRF observation (Fig 5D–I). In addition, we found that Zn was deposited in the maternal tissues next to the BETL of the kernels carrying homozygous *zmysl2-1* (Fig 5D–H). ICP-MS data also showed that the Zn concentrations in the adjacent maternal tissues of the mutant kernels were notably higher than those in the wild-type kernels (Fig 5J–L). These data further confirmed that ZmYSL2 functions in transporting Zn-NA from maternal tissues to filial BETLs. However, Zn deposition in the adjacent maternal tissues of the mutant kernels disappeared in the mature stage, suggesting that the deposited Zn might be recirculated to the mother plant (Figs 4I and 2H–J). Moreover, we did not observe Fe deposition in the adjacent maternal tissues of the mutant kernels, either in ICP-MS data (Fig EV4A–I) or in μXRF results (Fig EV4J–L), further indicating that Fe is not transported to the kernel via the same pathway as Zn.

Overexpression of *ZmYSL2* increases the Zn content in maize kernels

To further explore the application potential of *ZmYSL2*, we generated three independent transgenic maize lines with a construct of *pBETL9::ZmYSL2* that specifically overexpressed *ZmYSL2* in the BETL using *ZmBETL9* promoter (Zhan *et al*, 2015; Fig EV5A and B) and three lines with a construct of *pUbi::ZmYSL2* that constitutively overexpressed *ZmYSL2* (Fig EV5C and D). Elemental analysis and μXRF observation showed that the Zn contents in the kernels of the transgenic lines either constitutively overexpressing *ZmYSL2* or overexpressing *ZmYSL2* specifically in the BETL were significantly increased (Fig 6A, C, E, and F and Table 6). Among the overexpression lines, *pUbi::ZmYSL2-1* accumulated Zn at 39.9 mg kg^{-1} (Fig 6C and Table 7), which was 31.6% higher than that in the wild type and 20% higher than the breeding goal for Zn biofortification (33 mg kg^{-1}) (Bouis & Welch, 2010).

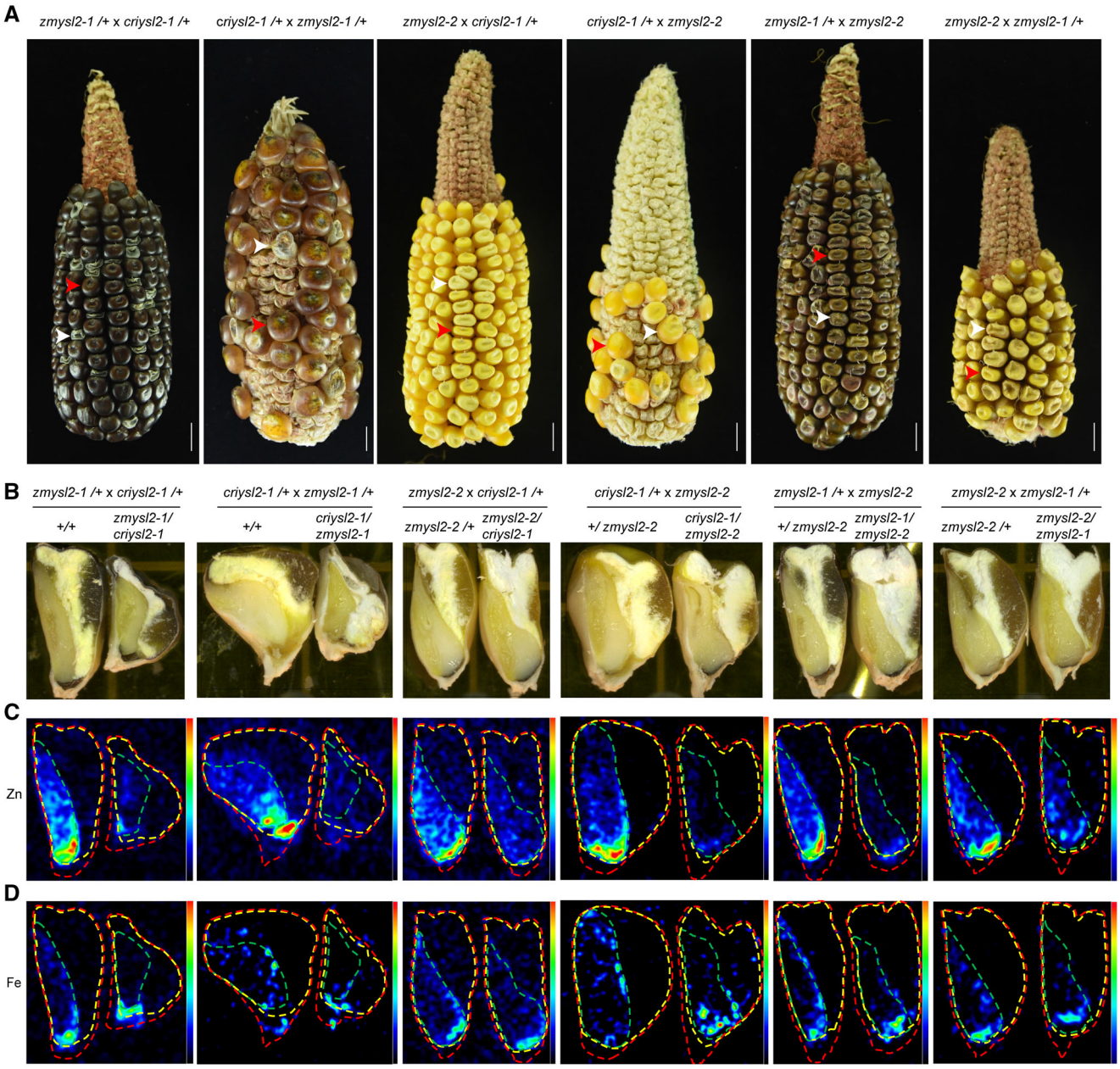

Figure 3. Allele test of the *criysl2*, *zmysl2-1*, and *zmysl2-2* alleles.

A Images of reciprocally pollinated ears among heterozygous *criysl2-1*, *zmysl2-1*, and homozygous *zmysl2-2* plants. The white arrow indicates genotyped homozygous *ysl2* mutant kernels and the red arrow indicates corresponding genotyped wild-type kernels. Scale bars, 1 cm.

B Images of genotyped mature kernels of reciprocally pollinated homozygous *ysl2* mutants and corresponding heterozygous *ysl2* and wild-type seeds.

C–D µXRF analysis of the Zn and Fe content and distribution in genotyped mature kernels of reciprocally pollinated homozygous *ysl2* mutants and corresponding heterozygous *ysl2* and wild-type seeds. The dashed line depicts different parts of the kernel, where the red line indicates the whole kernel, the yellow line indicates the embryo and endosperm, and the green line indicates the embryo.

Constitutive overexpression of *ZmYSL2* also led to an increase in the Fe level in the kernels but to a lesser extent (Fig 6D and Table 7) while specific overexpression of *ZmYSL2* in the BETL did not affect kernel Fe concentration (Fig 6B), suggesting that the increased Fe in the kernels of the constitutive overexpression transgenic lines was most likely due to ectopic effect of *ZmYSL2*. Consistent with this, the leaf Fe and Zn concentrations were also increased in the *pUbi::ZmYSL2* transgenic lines but not in the *pBETL9::ZmYSL2* transgenic lines (Fig EV5E–H). Interestingly, we did not observe any other phenotypic changes in the *ZmYSL2* overexpression lines in addition to the changes in the Zn and Fe levels (Fig EV5I–K). These data strongly imply that *ZmYSL2* has great potential to resolve the Zn-deficiency problem associated with cereal-based food.

Table 5. Allele test of the *ysl2* mutants.

Ear	+/+ and +/− (high Zn and normal endosperm)	*ysl2*/− (low Zn and opaque endosperm)	Observed ratio	Expected ratio	*P*-value for Chi-square test
zmysl2-1 /+ x *criysl2-1* /+	171	54	3.17:1	3:1	0.80
criysl2-1 /+ x *zmysl2-1* /+	52	16	3.25:1	3:1	0.95
zmysl2-2 x *criysl2-1* /+	99	105	0.94:1	1:1	0.77
criysl2-1 /+ x *zmysl2-2*	23	21	1.09:1	1:1	0.83
zmysl2-1 /+ x *zmysl2-2*	104	109	0.95:1	1:1	0.81
zmysl2-2 x *zmysl2-1* /+	64	58	1.1:1	1:1	0.70

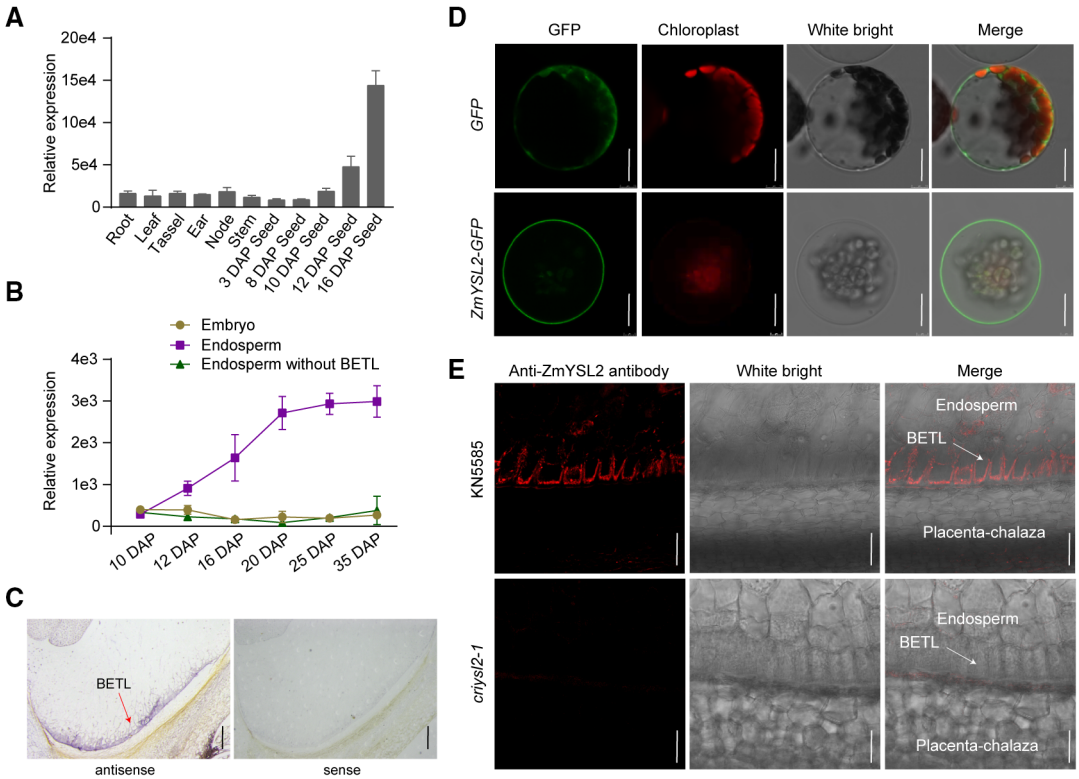

Figure 4. *ZmYSL2* is specifically localized on the plasma membrane facing the maternal tissue of the BETL.

A qRT–PCR analysis of *ZmYSL2* during seed development. Error bars represent the standard deviations from three biological replicates. DAP, day after pollination. $n = 3$ biological replicates.

B qRT–PCR analysis of *ZmYSL2* in embryos, endosperm, and endosperm without BETL during seed development. BETL, basal endosperm transfer layer. Error bars represent the standard deviations from three biological replicates. DAP, day after pollination. $n = 3$ biological replicates.

C RNA *in situ* hybridization of ZmYSL2 in seeds at 16 DAP in B73. Positive signals (indicated by the red arrow) are clearly restricted to BETL cells. No signals were observed in the negative control material. Scale bar, 500 μm.

D Subcellular localization of ZmYSL2 revealed by transiently expressing *ZmYSL2-GFP* in *Arabidopsis* mesophyll protoplasts using the *pA7* vector. *pA7-GFP* was used as a vector control. Scale bar, 20 μm.

E Immunofluorescence assays of *ZmYSL2* in seeds at 20 DAP in KN5585 and *criysl2-1*. Scale bar, 500 μm.

Source data are available online for this figure.

Discussion

The transport of nutrients into seeds is an essential process for seed development and plant reproduction, as well as for human nutrition. It has been reported that AtHMA2 and AtHMA4 are responsible for the unloading of Zn from the maternal tissue in *A. thaliana* (Olsen *et al*, 2016), but how Zn is uploaded to the filial tissue in plants remains unclear. In this study, we revealed that ZmYSL2 is the major transporter responsible for loading Zn to filial tissues in maize, filling a major gap in the knowledge regarding Zn homeostasis in plants and broadening our understanding of the molecular mechanisms underlying nutrient delivery from the mother plant to

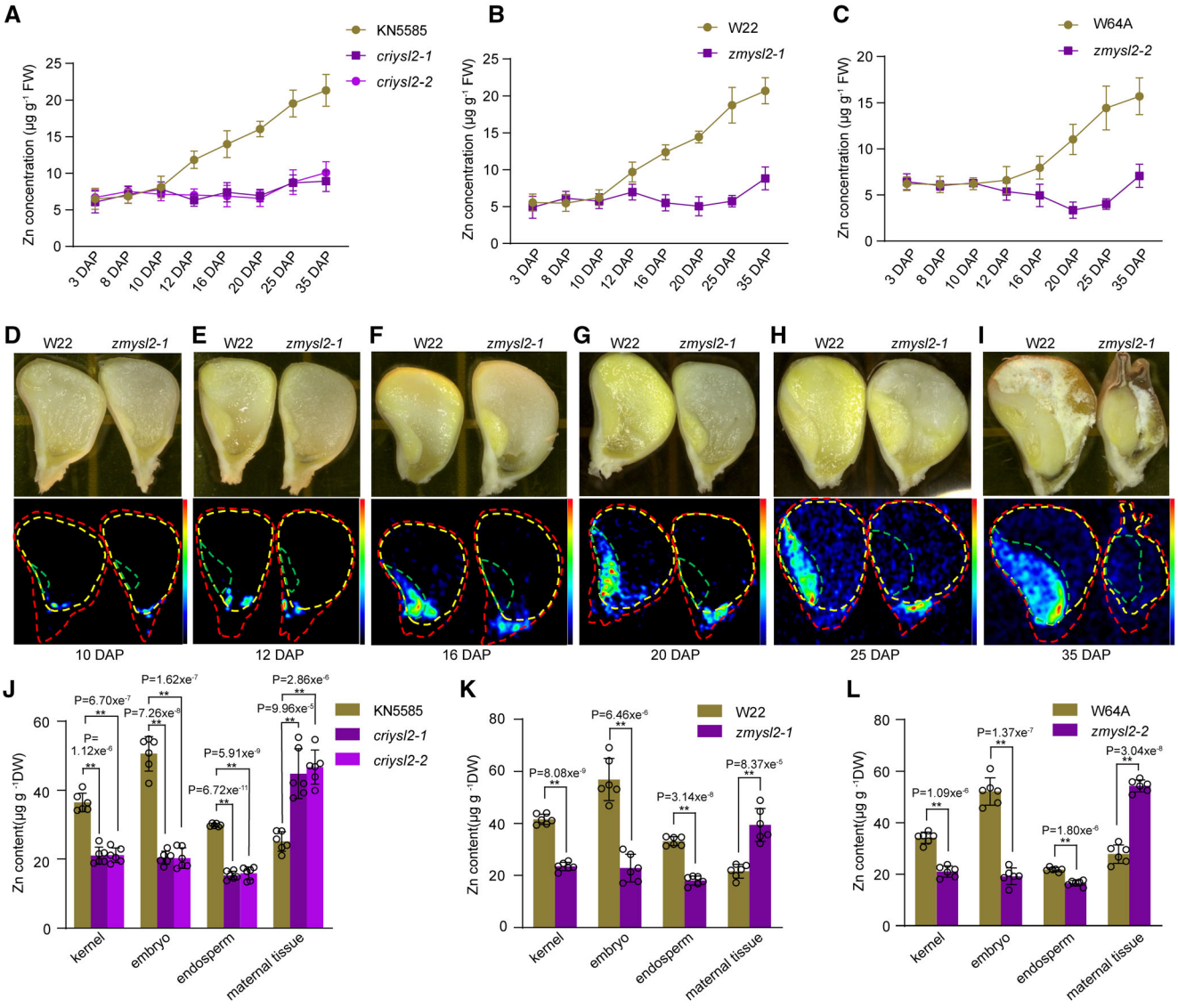

Figure 5. *ZmYSL2* is responsible for loading Zn from the maternal tissue into the BETL.

A–C Zn concentration in the *criysl2-1*(A), *criysl2-2*(A), *zmysl2-1* (B), and *zmysl2-2* (C) mutants during seed development. Fresh kernels of each genotype on different days after pollination were weighed and examined by ICP-MS after genotyping. Error bars represent the standard deviations from six biological replicates. DAP, day after pollination.

D–I μXRF analysis of the Zn distribution in kernels of W22 and homozygous *zmysl2-1* mutants during seed development. The dashed line depicts different parts of the kernel, where the red line indicates the whole kernel, the yellow line indicates the embryo and endosperm, and the green line indicates the embryo. DAP, day after pollination.

J–L Zn content in different parts of homozygous *criysl2-1* (J), *criysl2-2* (J), *zmysl2-1* (K), and *zmysl2-2* (L) seeds and the corresponding wild-type genotypes at 20 DAP. Genotyped fresh kernels of each genotype at 20 DAP were first dissected into different parts, including the whole kernel, embryo, endosperm, and maternal tissue, and then weighed, followed by ICP-MS analysis after drying. The data represent the means ± SDs. $n = 6$ biological replicates. $^{**}P < 0.001$ (Student's *t*-test).

Source data are available online for this figure.

the offspring (Fig 6G). In addition, *ZmYSL2* is also the first characterized mineral nutrient transporter specifically expressed in BETL, which not only supports the essential function of BETL in nutrient transport but also provides a marker for BETL.

Our data and previous studies showed that ZmYSL2 functions as a Zn-NA transporter (Zang *et al*, 2020; He *et al*, 2021), and the finding that ZmYSL2 dominates the mother-to-offspring transport of Zn thus suggests that Zn is transported into the seeds in the form of Zn-NA complexes. However, AtHMA2 and AtHMA4 export the ionic form of Zn out of the maternal tissue in *A. thaliana* (Olsen *et al*, 2016). Therefore, if maize employs the same Zn unloading strategy as *A. thaliana*, there must exist a chelation process for forming Zn-NA complexes at the maternal–filial interface. In this case, it would be interesting to study which one of HMAs and ZmYSL2 is the

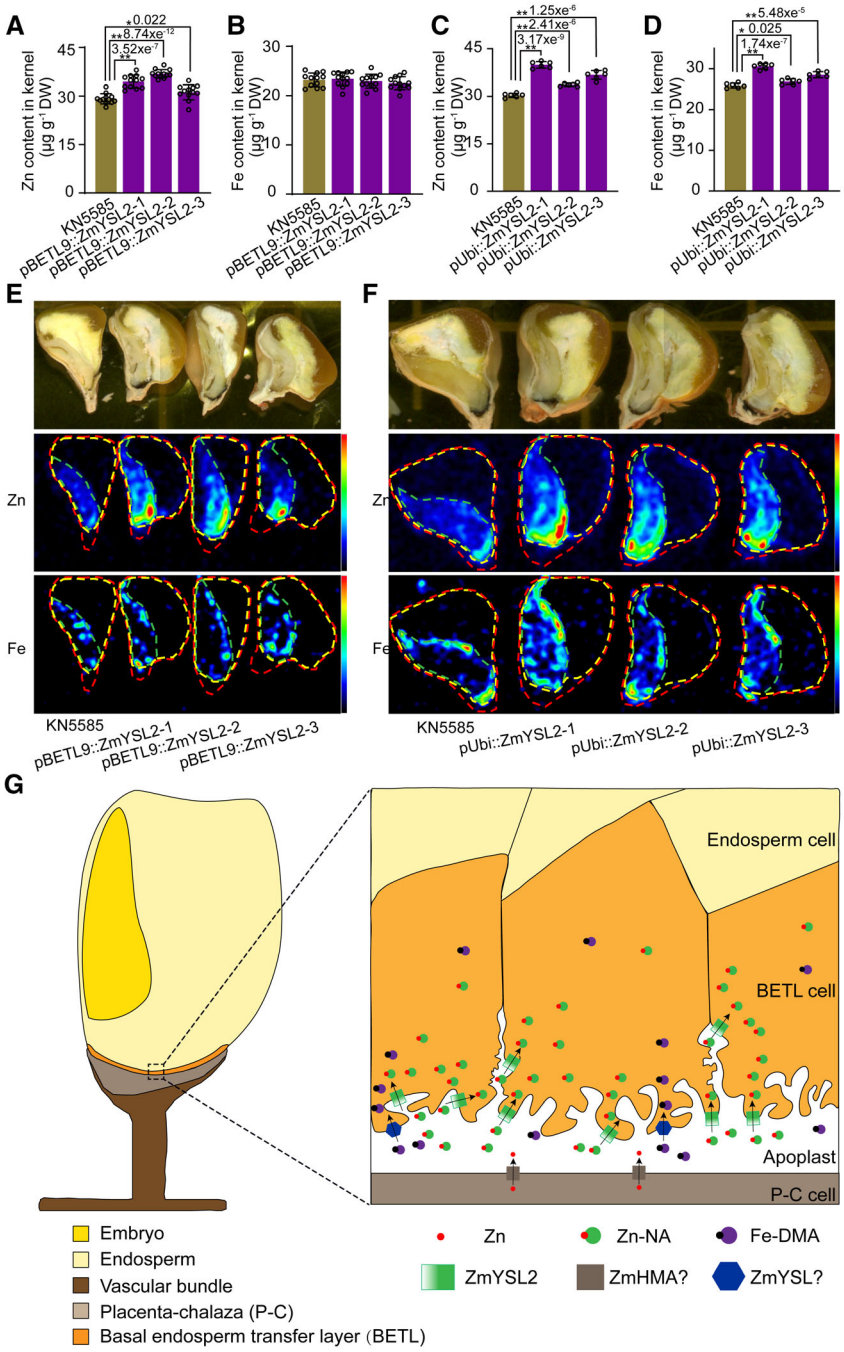

Figure 6. Overexpression of *ZmYSL2* increases the Zn content in maize kernels.

A–D Zn (A, D) and Fe (B, D) concentrations in the kernels of KN5585, three independent *pBETL9::ZmYSL2*^{B73} transgenic lines (A, B), and three *pUbi:ZmYSL2*^{B73} transgenic lines (C, D). Error bars represent the means ± SDs. $n = 6$–12 biological replicates. The different lowercase letters above the bars indicate significant differences by one-way ANOVA ($P < 0.01$) (K–M). $^{**}P < 0.001$ (Student's *t*-test). $n = 6$ biological replicates.

E–F μXRF analysis of the Zn and Fe content and distribution in mature kernels of KN5585, three *pBETL9::ZmYSL2*^{B73} transgenic lines (E), and three independent *pUbi:ZmYSL2*^{B73} transgenic lines (F). The dashed line depicts different parts of the kernel, where the red line indicates the whole kernel, the yellow line indicates the embryo and endosperm, and the green line indicates the embryo. The photograph and SAXF images shown in (E) and (F) represent composite images generated by the TORNADO system.

G Proposed model of ZmYSL2 function in maize kernel. ZmYSL2 is specifically localized on the plasma membrane facing the maternal tissue of the basal endosperm transfer cell layer (BETL) and functions in loading Zn-NA into the BETL. Fe-DMA complexes were transported into BETL by an unknown transporter. An HMA transporter may function in the export of free Zn from maternal tissue to the maternal–filial interface.

Source data are available online for this figure.

Table 6. Kernel element profile of KN5585 and *ZmYSL2* overexpression lines driven by *pBETL9* promoter.

Element	Content (μg g DW^{-1})				Percentage difference from KN5585 (%)			*P*-values
	KN5585	pBETL9:: ZmYSL2-1	pBETL9:: ZmYSL2-2	pBETL9:: ZmYSL2-3	pBETL9:: ZmYSL2-1	pBETL9:: ZmYSL2-2	pBETL9:: ZmYSL2-3	
B	13.16 ± 1.63	13.14 ± 1.29	13.15 ± 2.63	12.73 ± 2.15	−0.21	−0.13	−3.34	ns
Na	11.66 ± 2.28	11.21 ± 1.63	10.87 ± 1.76	10.60 ± 1.81	−3.84	−6.74	−9.08	ns
Mg	1045.55 ± 155.24	941.01 ± 140.40	940.25 ± 170.97	1023.88 ± 119.05	−10.00	−10.07	−2.07	ns
P	4175.04 ± 569.72	3813.68 ± 400.45	3934.58 ± 326.75	4283.34 ± 416.46	−8.66	−5.76	2.59	ns
S	568.28 ± 41.60	581.12 ± 57.89	539.43 ± 47.28	565.46 ± 76.81	2.26	−5.08	−0.50	ns
K	5367.44 ± 478.15	5146.50 ± 649.68	5158.04 ± 468.23	5407.55 ± 314.52	−4.12	−3.90	0.75	ns
Ca	198.44 ± 50.06	201.67 ± 38.78	199.49 ± 31.58	206.26 ± 51.62	1.63	0.53	3.94	ns
Ti	203.33 ± 52.34	200.94 ± 46.45	190.46 ± 61.81	211.44 ± 39.89	−1.18	−6.33	3.99	ns
Cr	0.32 ± 0.07	0.36 ± 0.06	0.34 ± 0.07	0.34 ± 0.04	12.08	6.06	7.11	ns
Mn	9.35 ± 1.36	9.24 ± 1.24	9.29 ± 1.38	9.77 ± 1.24	−1.16	−0.64	4.43	ns
Fe	23.2 ± 1.38	23.39 ± 1.40	22.94 ± 1.39	22.52 ± 1.31	0.83	−1.10	−2.94	**ns**
Co	**0.0031 ± 0.0005**	**0.0048 ± 0.0008**	**0.0065 ± 0.0006**	**0.0038 ± 0.0009**	**53.31**	**104.87**	**21.95**	**< 0.03**
Ni	0.11 ± 0.03	0.12 ± 0.03	0.11 ± 0.02	0.10 ± 0.03	5.54	−0.62	−7.07	ns
Cu	2.78 ± 0.50	2.83 ± 0.34	2.68 ± 0.28	2.82 ± 0.44	1.77	−3.42	1.36	**ns**
Zn	**29.18 ± 1.59**	**34.45 ± 2.00**	**36.85 ± 1.29**	**31.18 ± 2.32**	**18.05**	**26.27**	**6.83**	**< 0.02**
As	0.15 ± 0.02	0.15 ± 0.03	0.15 ± 0.02	0.15 ± 0.02	0.29	0.14	−1.10	ns
Se	2.53 ± 0.39	2.38 ± 0.49	2.69 ± 0.53	2.48 ± 0.42	−5.87	6.35	−2.13	ns
Rb	1.59 ± 0.13	1.53 ± 0.18	1.63 ± 0.20	1.50 ± 0.21	−3.90	2.81	−5.35	ns
Sr	0.62 ± 0.08	0.56 ± 0.08	0.58 ± 0.08	0.59 ± 0.06	−9.47	−5.76	−4.47	ns
Mo	0.17 ± 0.02	0.18 ± 0.03	0.17 ± 0.02	0.17 ± 0.02	2.63	−0.88	−0.13	ns
Cd	0.05 ± 0.008	0.06 ± 0.008	0.06 ± 0.007	0.06 ± 0.007	0.77	−3.67	−2.16	ns
Pb	3.83 ± 1.60	4.57 ± 0.78	3.76 ± 1.70	3.49 ± 1.02	19.18	−2.03	−8.82	ns

Data represent the mean ± SD ($n = 12$). Data in bold represent elements with a significant difference ($P \leq 0.05$) between the overexpression lines and KN5585 in three independent lines. ns, not significant. Statistical significance was determined by Student's *t*-test. Source data are available online for this Table.

bottleneck for mother-to-offspring transport of Zn, as it could be used for further improving Zn biofortification. Otherwise, the mother-to-offspring delivery mechanism of Zn should be different between maize and *A. thaliana*. Consistent with the latter possibility, we recently found that impaired NA secretion in *A. thaliana* does not affect seed Zn levels (Chao *et al*, 2021), while other studies found that Zn-NA is enriched in the phloem of cereal plants and is essential for Zn accumulation in the seeds of the cereal plants (Nishiyama *et al*, 2012). However, much more research should be conducted to prove or falsify these hypotheses.

ZmYSL2 also transports Fe-NA *in vivo* (Zang *et al*, 2020; He *et al*, 2021). Surprisingly, the loss of function of *ZmYSL2* did not affect the total Fe content in the kernel, and the weak allele *zmysl2-2* did not affect Fe distribution in the kernel. These data suggested that there is mechanistic divergence in the transport of Fe and Zn from the mother plant to the seeds. Consistent with this hypothesis, Fe was found to be mainly present in rice phloem sap in the form of Fe(III)-DMA, while Zn was present mainly in the form of Zn-NA (Nishiyama *et al*, 2012). In addition, DMA concentration rather than NA concentration is essential for Fe accumulation in cereal seeds (Diaz-Benito *et al*, 2018; Chao & Chao, 2022). Furthermore, we found that ZmYSL2 is not able to transport Fe(III)-DMA. These data together suggest that Fe might be loaded into the BETL in the form of Fe(III)-DMA through some other YSLs. However, it is possible that Fe(II)-NA is important for the distribution of Fe between embryo and endosperm, given that the null allele of *ZmYSL2* may affect the total NA content in kernels. This hypothesis is worthy of further study to address the complexity of Fe homeostasis in seeds.

Previous studies claimed that the opaque phenotype of the kernels of *ZmYSL2* mutants could be attributed to the disorder of Fe distribution in the kernels (Zang *et al*, 2020; He *et al*, 2021). This hypothesis was falsified by our identification of the weak allele *zmysl2-2*, which produced opaque kernels but exhibited a normal Fe distribution. Instead, the opaque phenotype of the *ZmYSL2* mutant kernels most likely resulted from a lack of Zn, given that Zn is required for starch and protein synthesis (Jyung & Ehmann, 1975; Broadley *et al*, 2007) and that all kernels with impaired *ZmYSL2* were low in Zn. Fe is more likely to be required for embryo development, given that only the knockout mutants of *ZmYSL2* were not viable. Consistent with this, a lack of Fe in the seeds of *A. thaliana* also caused severe defects in embryo development and seed germination (Klatte *et al*, 2009; Chu *et al*, 2010; Chao *et al*, 2021). This study thus also contributes to our understanding of the role of trace elements in seed development.

Table 7. Kernel element profile of KN5585 and *ZmYSL2* overexpression lines driven by *Ubi* promoter.

Element	Content (μg g DW^{-1})				Percentage difference from KN5585 (%)			*P*-values
	KN5585	pUbi::ZmYSL2-1	pUbi::ZmYSL2-2	pUbi::ZmYSL2-3	pUbi::ZmYSL2-1	pUbi::ZmYSL2-2	pUbi::ZmYSL2-3	
B	9.10 ± 1.25	8.94 ± 1.03	8.95 ± 1.16	9.27 ± 0.63	−1.81	−1.65	1.88	ns
Na	9.94 ± 0.80	10.13 ± 0.74	10.29 ± 0.45	9.24 ± 0.93	1.92	3.53	−7.05	ns
Mg	1133.87 ± 64.48	1104.17 ± 45.57	1129.21 ± 29.75	1128.82 ± 33.50	−2.62	−0.41	−0.45	ns
P	4077.23 ± 179.30	4275.37 ± 188.26	4321.80 ± 230.65	4112.21 ± 328.26	4.86	6.00	0.86	ns
S	656.61 ± 28.81	640.87 ± 24.43	664.11 ± 21.81	627.49 ± 27.11	−2.40	1.14	−4.43	ns
K	4325.04 ± 220.48	4395.61 ± 186.76	4414.65 ± 161.91	3999.06 ± 238.04	1.63	2.07	−7.54	ns
Ca	167.19 ± 54.13	197.13 ± 19.25	176.81 ± 43.33	176.88 ± 49.17	17.91	5.76	5.79	ns
Ti	85.87 ± 9.24	77.80 ± 12.57	84.86 ± 14.69	80.97 ± 17.86	−9.39	−1.18	−5.70	ns
Cr	0.31 ± 0.04	0.31 ± 0.02	0.31 ± 0.01	0.30 ± 0.01	1.08	1.46	−4.78	ns
Mn	8.91 ± 1.00	11.07 ± 1.17	10.19 ± 0.88	10.00 ± 1.38	24.36	14.44	12.27	ns
Fe	**25.90 ± 0.60**	**30.59 ± 0.68**	**26.86 ± 0.67**	**28.53 ± 0.75**	**18.13**	**3.72**	**10.15**	**< 0.02**
Co	**0.0032 ± 0.0006**	**0.0094 ± 0.0011**	**0.0055 ± 0.0003**	**0.0079 ± 0.0008**	**188.28**	**69.53**	**140.60**	**< 0.0006**
Ni	0.11 ± 0.01	0.11 ± 0.01	0.10 ± 0.01	0.11 ± 0.01	0.36	−2.08	−0.76	ns
Cu	**1.62 ± 0.17**	**2.41 ± 0.26**	**1.83 ± 0.15**	**2.14 ± 0.25**	**48.52**	**12.83**	**32.03**	**< 0.04**
Zn	**30.33 ± 0.65**	**39.92 ± 1.03**	**33.66 ± 0.55**	**36.75 ± 1.37**	**31.61**	**10.97**	**21.16**	**< 0.0006**
As	0.11 ± 0.01	0.12 ± 0.01	0.11 ± 0.01	0.11 ± 0.01	6.86	1.67	−0.03	ns
Se	1.70 ± 0.29	1.68 ± 0.24	1.75 ± 0.21	1.58 ± 0.21	−1.25	−3.22	−7.70	ns
Rb	1.94 ± 0.23	2.03 ± 0.17	1.81 ± 0.10	1.89 ± 0.15	4.35	−6.82	−2.37	ns
Sr	0.61 ± 0.05	0.64 ± 0.06	0.59 ± 0.04	0.60 ± 0.07	6.20	−3.12	−0.53	ns
Mo	0.13 ± 0.01	0.13 ± 0.01	0.12 ± 0.01	0.14 ± 0.01	4.75	−3.23	5.58	ns
Cd	0.06 ± 0.005	0.06 ± 00006	0.05 ± 0.004	0.06 ± 0.004	−5.43	−8.86	1.02	ns
Pb	2.29 ± 0.31	2.13 ± 0.24	2.50 ± 0.34	2.09 ± 0.44	−6.94	9.12	−8.67	ns

Data represent the mean ± SD ($n = 6$). Data in bold represent elements with a significant difference ($P \leq 0.05$) between the overexpression lines and KN5585 in three independent lines. ns, not significant. Statistical significance was determined by Student's *t*-test. Source data are available online for this Table.

Breeding high-Zn crops, which relies on the genetic diversity of the crops, is one of the most important strategies to achieve Zn biofortification. Although previous studies have uncovered the rich genetic diversity controlling the natural variation in the Zn content of maize kernels (Baxter *et al*, 2013; Maqbool & Beshir, 2019), none of the QTLs had been cloned. The power of GWAS allowed us to identify *ZmYSL2* as the first successfully cloned QTL controlling natural variation in mineral nutrients in maize kernels, and these findings will aid the identification of additional ionome-related QTLs in maize by using GWAS.

The polymorphisms of *ZmYSL2* associated with the maize kernel's Zn content represent important and reliable molecular markers to assist in the breeding of high-Zn maize varieties. These findings will also aid the engineering of high-Zn maize via enhancement of the expression of *ZmYSL2*. Overexpression of *ZmYSL2* driven by the *Ubi* promoter confirmed that this idea is feasible, as we have shown that this strategy was able to increase the Zn content in kernels to 31.6% higher than that in wild-type kernels and 20% higher than the breeding goal of Zn biofortification for maize. In addition, overexpression of *ZmYSL2* driven by the BETL-specific promoter *pBETL9* was also able to significantly enhance Zn accumulation in kernels, but the increase was slightly lower than that of the constitutive overexpression lines. These data suggest that overexpression of *ZmYSL2* in the roots might also contribute to the increase of Zn in the kernels. However, it is hard to estimate how constitutive overexpression of *ZmYSL2* contributes to the final increase in the kernel Zn as ectopic expression of *ZmYSL2* might also lead to more distribution of Zn to other tissues such as leaves. Thus, it will be good to evaluate the effectiveness of more promoters in enhancing the expression of *ZmYSL2* and Zn accumulation in kernels.

Material and Methods

Plant material and growth conditions

The two knockout mutants *criysl2-1* and *criysl2-2* were generated by CRISPR/Cas9 technology in the KN5585 background. The allele *zmysl2-1* was obtained from the UniformMu Transposon Resource. The allele *zmysl2-2* was obtained from EMS mutagenesis in the W64A background. The *ZmYSL2* overexpression lines were obtained from transgenic events in the KN5585 background separately using *pBETL9::*

ZmYSL2^{B73} and *pUbi::ZmYSL2*^{B73} platforms. The complete-diallel design plus unbalanced breeding-like inter-cross (CUBIC) population (Liu *et al*, 2020b) derived from extensive intercrosses of 24 elite Chinese maize inbred lines was planted in a nursery field at Sanya, Hainan (2016, winter). All maize plants were planted in one-row plots (2.5 m per row with 0.25 m spacing between plants and 0.75 m between rows) in each location. Field management followed standard procedures. The mutants and T_3-generation overexpression lines were planted in a nursery field in Songjiang, Shanghai (2020 and 2021, summer).

Vector construction

To generate mutants of *criysl2-1* and *criysl2-2*, two sgRNAs targeting *ZmYSL2* (AAGGTGCGGGCAGATCATCC and AGCTGGTCATGCTGCTCTC) were inserted into the binary vector *pCPB-ZmUbi::hSpCas9* vector (Li *et al*, 2017). To construct the *ZmYSL2* overexpression vectors, the coding region of *ZmYSL2* was amplified from endosperm cDNA in B73 and inserted into the *proZmUbi::eYFP* vector to generate the *pUbi::ZmYSL2*^{B73} constructs. To construct the expression vectors *pBETL9::ZmYSL2*^{B73}, CDS fragment of ZmYSL2 was amplified from B73 cDNA using the primers pBETL9-ZmYSL2-ov-F/pTF102-ZmYSL2-R. The 2 kb fragment of ZmBETL9 promoter was amplified from B73 genomic DNA using the primers pTF102-pBETL9-F/pBETL9-ZmYSL2-ov-R. Thereafter, two fragments were fused by overlapping PCR with the primers pTF102-pBETL9-F and pTF102-ZmYSL2-R. The fused fragment was inserted into the cloning site between Spe I and Pst I of the binary expression vector *pTF102-p27* by using the Hieff Clone one-step PCR Cloning kit (Yisheng Co. Ltd, Shanghai, China). Both the gene-editing and overexpression constructs were transferred to the *Agrobacterium* strain EHA105 and transformed into the immature embryo of the maize inbred line KN5585 (Liu *et al*, 2020a) through *Agrobacterium*-mediated transformation by WIMI Biotechnology Co., Ltd.

For the construction of the yeast expression vector *pDR196-ZmYSL2* for different genotypes, the coding region of *ZmYSL2* was amplified from endosperm cDNA in HuangC, HZS, Lv28, YFH, W64A, or *zmysl2-2* by using the primers pDR196-ZmYSL2-F and pDR196-ZmYSL2-R. For the construction of the yeast expression vector *pDR196-OsYSL15*, the coding region of *OsYSL15* was amplified from cDNA in *Oryza sativa* cv. Nipponbare by using the primers pDR196-OsYSL15-F and pDR196-OsYSL15-R. For the construction of the yeast expression vector *pDR196-AtIRT1*, the coding region of *AtIRT1* was amplified from the cDNA of Col-0 by using the primers pDR196-AtIRT1-F and pDR196-AtIRT1-R. For the construction of the yeast expression vector *pDR196-ZmYS1*, the coding region of *ZmYS1* was amplified from the cDNA of B73 by using the primers pDR196-ZmYS1-F and pDR196-ZmYS1-R. Each amplified fragment was cloned into the cloning site between *Spe* I and *Xho* I of the yeast expression vector *pDR196*.

To construct the transient expression vectors of *pA7-ZmYSL2-GFP*, the coding regions of *ZmYSL2* without the stop codon from B73 were amplified and inserted into the pA7-GFP vector. The primers used are listed in Table 8.

Elemental profiling

The elemental analysis was conducted by inductively coupled plasma mass spectrometry (ICP-MS) as previously described (Danku *et al*, 2013). For mature kernels of CUBIC individuals, 10 dry mature kernels of each maize line were ground into powder by a customized grinder with a grinding tank (material: polytetrafluoroethylene) and beads (material: Jargonia) manufactured by Jingxin Industry Co., Ltd., Shanghai. For mature kernels of mutants and overexpression lines, after harvest, kernels were detached from the same or different ears and grouped based on seed phenotype and genotype, and at least six kernels were ground into powder using the method described above. Then, 2–5 mg of each sample was used for ICP-MS analysis. To investigate the element changes that occurred during kernel development, each fresh kernel (20 days after pollination [DAP]) was sampled for weighing and then dried for ICP-MS analysis. To detect the ionome in different parts of 20 DAP seeds, genotyped fresh kernels of each genotype at 20 DAP were first dissected into different parts, including the whole kernel, embryo, endosperm, and maternal tissue, and then weighed, followed by ICP-MS analysis after drying. The maternal tissue indicates an area in the kernel excluding the embryo and endosperm that is close to BETL.

The powdered samples were placed into Pyrex test tubes (16 × 100 mm) to dry in an oven at 65°C for 24 h. After weighing 12 samples (these weights were used to calculate the weights of the rest of the samples), Primar Plus nitric acid for trance metal analysis (Fisher Chemicals) spiked with an indium internal standard was added to the tubes (1 ml per tube). The samples were then digested in a block heater (DigiPREP MS, SCP Science; QMX Laboratories, Essex, UK) at 115°C for 5 h. The digested samples were diluted to 10 ml with 18.2 MΩ Milli-Q Direct water (Merck Millipore). Elemental analysis was performed using ICP-MS (NexION 350D; PerkinElmer, USA) coupled with an Apex desolvation system and an SC-4 DX autosampler (Elemental Scientific Inc., USA). All the solid samples were normalized with a heuristic algorithm using the best-measured elements as previously described (Lahner *et al*, 2003).

For each set of ICP-MS measurements of CUBIC individuals, the median value from each run was used to correct run-to-run variations. The corrected values were then log2 transformed for genome-wide association analysis.

Genome-wide association study

A genome-wide association study (GWAS) was performed using 10.8 million SNPs (MAF ≥ 0.05) in the CUBIC population. The same relatedness matrix and the top 10 PCs used in the previous study (Liu *et al*, 2020b) accounting for the familial relationship (K) and population structure (Q) were routinely fitted into the mixed linear model (MLM) of TASSEL 5.0 (Bradbury *et al*, 2007). The significance threshold for the association was determined to be 9.3 e-08 according to the Bonferroni correction ($P = 1/n$; n = total markers used for GWAS).

Functional complementation assay in yeast

The *pDR196-ZmYSL2* vector for different genotypes, including HuangC, HZS, Lv28, and YFH, and *pDR196-OsYSL15* as well as the pDR196 empty vector were introduced into the *zrt1zrt2* (MATa, *his3*, *leu2*, *met1*, *lys2*, *ura3*, *zrt1*, *zrt2*) yeast strain. The *pDR196-ZmYSL2* vector for different genotypes, including W64A and zmysl2-2 and *pDR196-AtIRT1*, *pDR196-ZmYS1*, as well as the

Table 8. Primers used in this study.

Use	Primer name	Primer sequence (5′-3′)
qRT for ZmYSL2	qZmYSL2-F	GCCAGCTTCGCCATCGACAT
	qZmYSL2-R	CTAGCTTCCAGGTGTAAATTTC
qRT for Zm00001d044172	W130-F	CGTCCACCCATAGTGCCATGAG
	W130-R	ACGGCAAGTAGCACTCAGACAC
Haplotype analysis	Hap1-ProZmYSL2-F	TAAATCGTCTCCGACCCACAG
	Hap2-ProZmYSL2-F	TAACGGCTCATCCACTTCCG
	Hap3-ProZmYSL2-F	CTCCCAAACCGGCGATACTT
	Hap4-ProZmYSL2-F	ACCCCTTTCGGCCTCTAGAA
	Hap-ProZmYSL2-R	GAGCAAGAACTACTATCAATCAG
ZmYSL2 RNA probes construct	ZmYSL2-anti-F	ATGCCGAGGACCACAACTCCAC
	ZmYSL2-anti-R	ATACGACTCACTATAGGGCGAACGGCGACGCCCAGGCGGGACA
pA7-ZmYSL2 construct	pA7-ZmYSL2-F	TTACGAACGATACTCGAGATGCCGAGGACCACAAC
	pA7-ZmYSL2-R	CCATCACTAGTACGTCGACGAAATTTACACCTGGAAGC
pDR196-ZmYSL2 construct	pDR196-ZmYSL2-F	ATCCCCCGGGCTGCAGGAATTCATGCCGAGGACCACAAC
	pDR196-ZmYSL2-R	GGTACCGGGCCCCCCCTCGAGCTAGCTTCCAGGTGTAAATTTC
pDR196-OsYSL15 construct	pDR196-OsYSL15-F	ATCCCCCGGGCTGCAGGAATTCATGGAGCACGCCGACGCGGAC
	pDR196-OsYSL15-R	GGTACCGGGCCCCCCCTCGAGTTAGCTTCCAGGCGTAAACTTCA
pDR196-AtIRT1 construct	pDR196-AtIRT1-F	ATCCCCCGGGCTGCAGGAATTCATGGCTTCAAATTCAGCACT
	pDR196-AtIRT1-R	GGTACCGGGCCCCCCCTCGAGTTAAGCCCATTTGGCGATAATC
pDR196-ZmYS1 construct	pDR196-ZmYS1-F	ATCCCCCGGGCTGCAGGAATTCATGGACCTTGCACGGAGCG
	pDR196-ZmYS1-R	GGTACCGGGCCCCCCCTCGAGCTAGCTTCCAGGAGTGAAC
pTF102-pBETL9::ZmYSL2 construct	pTF102-pBETL9-F	AGCAATGCACGGGCATATAACTAGTACACGCCCATGAAACCATGA
	pBETL9-ZmYSL2-ov-F	CGTCAACAGTTGAAGTTATACCCATGCCGAGGACCACAAC
	pBETL9-ZmYSL2-ov-R	GTTGTGGTCCTCGGCATGGGTATAACTTCAACTGTTGACG
	pTF102-ZmYSL2-R	GGTGATTTTTGCGCCGCTGCACTAGCTTCCAGGTGTAAATTTC

pDR196 empty vector were introduced into the *fet3fet4* (DEY1453, MATα, *ade2*, *can1*, *his3*, *leu2*, *trp1*, *ura3*, fet3::HIS3, fet4::LEU2) yeast strain. Transformed yeast cells were diluted from an optical density of 1 to 0.001 at 550 nm and spotted onto synthetic defined (SD)-Ura medium, in which YDB with low Zn and Fe was gotten from USBiological (L18022001). Chemically synthesized NA was purchased from Cayman Chemical, USA, and the DMA was kindly provided by Luqing Zheng. For the *zrt1zrt2* yeast strain, the medium was supplemented with 10 μM $ZnSO_4$ or 10 μM NA-$ZnSO_4$ at pH 7. For the *fet3fet4* yeast strain, the medium was supplemented with 0 μM $FeSO_4$, 10 μM $FeSO_4$, 10 μM NA-$FeSO_4$, 10 μM DMA-$FeCl_3$, and 100 μM $FeSO_4$ at pH 7. NA-$ZnSO_4$ was prepared according to the following protocol: 11 μl of 10 mM NA or DMA and 10 μl of 10 mM $ZnSO_4$ or $FeSO_4$ were mixed and incubated for 10 min at 60°C, and then, 10 ml of SD-Ura medium was added to the plates (von Wiren *et al*, 1999). NA-$FeSO_4$ was prepared by mixing 10 mM $FeSO_4$ in 20 mM sodium ascorbate with 5 mM NA solution and 200 mM MES/Tris buffer (pH 7.0) to produce 0.5 mM Fe, 2.5 mM NA, and 50 mM MES/Tris buffer, followed by 10 min incubation at 65°C. DMA-$FeCl_3$ was prepared by mixing 10 mM $FeCl_3$ in 10 mM HCl with 5 mM DMA and 200 mM MES/Tris buffer (pH 7.0) to produce 0.5 mM Fe, 2.5 mM DMA, and 50 mM MES/Tris buffer, followed by 3 h incubation at room temperature.

Micro-X-ray fluorescence visualization

The Zn and Fe distribution in the kernels of different maize genotypes was obtained using a microenergy-dispersive X-ray fluorescence (mEDXRF) system (M4 Tornado; Bruker, Germany). For mature kernels, seeds were cut in half by using a ceramic knife; half of the kernels were used for genotyping, and the other half were used for SXAF analysis. For immature kernels, fresh seeds were cut in half immediately by using a ceramic knife; half of the kernels were used for genotyping, and the other half were used for SXAF analysis within 10 min. Zn and Fe fluorescence was observed under Rh X-ray tube illumination. The X-ray generator was operated at 50 kV and 600 mA. For better visualization, a set of filters between the X-ray tube and the sample were used, which was composed of three foils of Al/Ti/Cu with thicknesses of 100/50/25 mm. The elemental mappings were performed with a pixel spacing of 30 μm to completely cover the kernel, with a measurement time of 2 ms per pixel.

For SXAF image larger than 14 mm × 11 mm, a mosaic image was recorded by M4 TORMADO. Like a microscope, the M4 TORNADO applies a simple imaging system, in which the position of the X-ray tube and camera is stationary, and the X–Y–Z stage can move to enable the exact focusing and positioning of the sample

required by the small spot of the excitation radiation. A 10× magnification camera with a field view of 14 mm × 11 mm was used for the overview of the sample. When the sample's size exceeds the field of view of the 10× camera, for ease of navigation and overview, the M4 TORNADO allows to create a so-called mosaic image, which can cover an area as large as the stage area.

RT–qPCR analysis

The roots, leaves, stems, silks, tassels, seeds, endosperms, and embryos from B73 plants were collected and flash-frozen in liquid nitrogen. The roots, leaves, stems, and nodes were collected at the L10 stage. Silks and tassels were collected at the plant flowering stage. The seeds, endosperm, and embryos were collected on different days after pollination. Total RNA was extracted by TRIzol reagent (Invitrogen, catalog number 15596018) and then purified with an RNeasy Mini Kit (Qiagen, catalog number 74106) after DNaseI digestion (Qiagen, catalog number 79254) following the manufacturer's protocol. For RT–qPCR analysis of *ZmYSL2* expression, digested RNA was used for reverse transcription with a Super Script III First Strand Kit (Invitrogen). The resulting cDNA was diluted to 50 ng μl^{-1} for RT–qPCR with SYBR Green (TOYOBO) on a CFX Connect Real-Time System (Bio-Rad). The maize gene (Zm00001d044172) was used as the internal control (Wang *et al*, 2018). The relative expression of the gene was calculated by the $2^{-\Delta C_t}$ method. All the experiments were performed with three independent RNA samples. Primers are listed in Table 8.

Subcellular localization of ZmYSL2

For transient expression of ZmYSL2 in *Arabidopsis* protoplasts, vectors were transferred into protoplasts of Col-0 following previously described methods (Wu *et al*, 2009). At 36 h after incubation, fluorescence signals were recorded under a Leica TCS SP8 confocal laser scanning microscope. To observe the GFP signals, an excitation wavelength of 488 nm from an argon laser was used, and the emission signal was detected at 500–550 nm.

RNA *in situ* hybridization

RNA *in situ* hybridization for ZmYSL2 was performed following the method described previously (Zhang *et al*, 2015) with modifications. At 16 DAP, seeds from the middle region of the KN5585 ears were harvested and fixed in 4% paraformaldehyde solution with 0.1% Triton X-100 and 0.1% Tween 20 in phosphate-buffered saline (PBS) (Takara, Cat# T900) overnight. The seeds were then dehydrated using a gradient concentration of ethanol and embedded in paraffin. A 400-bp cDNA fragment of *ZmYSL2* was amplified using the primer pair ZmYSL2-anti-F and ZmYSL2-anti-R. The antisense and sense RNA probes were synthesized according to the instructions for the DIG RNA Labeling Mixture (Roche Cat# 11175025910). Ten-micrometer seed sections were cut and then hybridized with the RNA probes at 50°C overnight. After blotting with anti-digoxigenin AP-conjugated antibody (Roche Cat# 11093274910) and incubation with NBT solution (Roche Cat# 11383213001), the sections were observed and photographed with an ECLIPSE 80i microscope.

Measurement of the proteins, starch, and phytic acid

Approximately 10 kernels were selected from the middle of each ear that had their embryo, seed coat, and aleurone removed. The resulting endosperm was dried in an oven at 60°C and then ground into fine powder by a customized grinder. The extraction and analysis of zein and non-zein proteins were conducted as previously described (Liu *et al*, 2016). For assaying the total protein content, 60 mg of endosperm powder was used for measurement by an ELEMENTAR Rapid N exceed instrument. The endosperm powder was filtered through an 80-mesh sieve to prepare samples for starch measurement. The starch content was measured with a Total Starch Assay kit (K-TSTA; Megazyme) following the standard protocol (Deng *et al*, 2020). Three biological replicates were performed. The phytic acid contents were measured by using a Total Phytic Acid Assay kit (K-PHYT; Megazyme) following the protocol provided by the manufacturer.

Immunostaining of ZmYSL2

ZmYSL2 antibodies were produced by ABclonal. The cDNA fragment encoding the partial ZmYSL2 protein from amino acids 1–90 was cloned into the prokaryotic expression vector pET-28a-ZmYSL2. Purified protein was injected into rabbits to produce ZmYSL2 antibodies. After affinity purification, the antibodies were used for immunofluorescence histochemistry.

Immunostaining of ZmYSL2 was performed following the method described previously (Huang *et al*, 2019) with modifications. In brief, hand-cut sections of 16 DAP seeds in KN5585 and *criysl2-1* were fixed for 1 h in freshly prepared 4% (v/v) formaldehyde in PHEM buffer (60 mM PIPES, 25 mM HEPES, 10 mM EGTA, and 2 mM $MgCl_2$; pH 6.9) with 0.02% (v/v) Triton X-100 and 5% (v/v) DMSO. After being rinsed several times in PHEM buffer, the samples were digested in an enzyme solution containing 1% (w/v) β-glucuronidase (LabTop, catalog number S10046), 0.1% (w/v) cellulose (Yakult, catalog number 9012-54-8), 0.1% (w/v) pectinase (LabTop, catalog number S10007), 0.1% (w/v) lyticase (Yeasen, catalog number 10403ES92), and 1% (w/v) glucose at 37°C for 30 min to remove cell walls, followed by washing with PHEM buffer. Samples were put into PHEM buffer with 1% Triton X-100, 5% DMSO, and 3% BSA (w/v) at 37°C for 30 min. After washing again with PHEM buffer, the samples were placed in PBS (10 mM Na_2HPO_4, 1.8 mM KH_2PO_4, 2.7 mM KCl, and 137 mM NaCl; pH 7.4) with anti-ZmYSL2 antibody (1:200) and incubated overnight in the dark at 4°C. Then, the samples were washed five times with PBS and incubated with Alexa Fluor 555-conjugated goat anti-mouse IgG secondary antibody at a dilution of 1:300 (Abmart, catalog number M213411M) in PBS for 1 h at 37°C. After washing five times in PBS, the samples were then observed using a confocal laser scanning microscope (TSC SP8 STED 3X, Leica). To observe the secondary antibody signals, an excitation wavelength of 555 nm from an argon laser was used, and the emission signal was detected at 565–590 nm.

Data availability

All data are present either in the main study or the supplementary materials. This study includes no data deposited in external repositories.

Expanded View for this article is available online.

Acknowledgements
We thank David E Salt for the critical reading of the manuscript. We thank Luqing Zheng for kindly providing us with DMA. We thank Rumei Chen for kindly providing yeast strains *zrt1zrt2* and *fet3fet4*. We thank Mingguang lei for his help with the phytic acid detection and Shuining Yin for her help with the microscope studies. This work was supported by the National Natural Science Foundation of China (31930024), Chinese Academy of Sciences (XDB27010103), and the Newton Fund (NAF\R1\201264).

Author contributions
Zhen-Fei Chao: Conceptualization; resources; data curation; software; formal analysis; validation; investigation; visualization; methodology; writing—original draft. **Yuan-Yuan Chen:** Conceptualization; resources; data curation; software; formal analysis; validation; investigation; visualization; methodology. **Chen Ji:** Conceptualization; data curation; formal analysis; validation; investigation; methodology. **Ya-Ling Wang:** Data curation; software; validation; methodology. **Xing Huang:** Data curation; formal analysis; investigation; methodology. **Chu-Ying Zhang:** Investigation; methodology. **jun Yang:** Investigation; methodology. **Tao Song:** Investigation; methodology. **Jia-Chen Wu:** Investigation; methodology. **Liang-XIng Guo:** Investigation; methodology. **Chu-Bin Liu:** Software; investigation. **Mei-Ling Han:** Data curation; investigation. **Yong-Rui Wu:** Conceptualization; supervision; writing—review and editing. **Jianbing Yan:** Conceptualization; supervision; writing—review and editing. **Dai-Yin Chao:** Conceptualization; data curation; formal analysis; supervision; funding acquisition; investigation; writing—review and editing.

Disclosure and competing interests statement
The authors declare that they have no conflict of interest.

References

Baxter IR, Gustin JL, Settles AM, Hoekenga OA (2013) Ionomic characterization of maize kernels in the intermated B73 x Mo17 population. *Crop Sci* 53: 208–220

Bouis HE, Welch RM (2010) Biofortification-a sustainable agricultural strategy for reducing micronutrient malnutrition in the global south. *Crop Sci* 50: S20–S32

Bradbury PJ, Zhang Z, Kroon DE, Casstevens TM, Ramdoss Y, Buckler ES (2007) TASSEL: software for association mapping of complex traits in diverse samples. *Bioinformatics* 23: 2633–2635

Broadley MR, White PJ, Hammond JP, Zelko I, Lux A (2007) Zinc in plants. *New Phytol* 173: 677–702

Chao ZF, Chao DY (2022) Similarities and differences in iron homeostasis strategies between graminaceous and nongraminaceous plants. *New Phytol* 236: 1655–1660

Chao ZF, Wang YL, Chen YY, Zhang CY, Wang PY, Song T, Liu CB, Lv QY, Han ML, Wang SS *et al* (2021) NPF transporters in synaptic-like vesicles control delivery of iron and copper to seeds. *Sci Adv* 7: eabh2450

Chu HH, Chiecko J, Punshon T, Lanzirotti A, Lahner B, Salt DE, Walker EL (2010) Successful reproduction requires the function of *Arabidopsis* yellow stripe-Like1 and yellow stripe-Like3 metal-nicotianamine transporters in both vegetative and reproductive structures. *Plant Physiol* 154: 197–210

Curie C, Panaviene Z, Loulergue C, Dellaporta SL, Briat JF, Walker EL (2001) Maize yellow stripe1 encodes a membrane protein directly involved in Fe (III) uptake. *Nature* 409: 346–349

Danku JM, Lahner B, Yakubova E, Salt DE (2013) Large-scale plant ionomics. *Methods Mol Biol* 953: 255–276

Deng Y, Wang J, Zhang Z, Wu Y (2020) Transactivation of Sus1 and Sus2 by Opaque2 is an essential supplement to sucrose synthase-mediated endosperm filling in maize. *Plant Biotechnol J* 18: 1897–1907

Diaz-Benito P, Banakar R, Rodriguez-Menendez S, Capell T, Pereiro R, Christou P, Abadia J, Fernandez B, Alvarez-Fernandez A (2018) Iron and zinc in the embryo and endosperm of Rice (*Oryza sativa* L.) seeds in contrasting 2′-Deoxymugineic acid/Nicotianamine scenarios. *Front Plant Sci* 9: 1190

Gashu D, Nalivata PC, Amede T, Ander EL, Bailey EH, Botoman L, Chagumaira C, Gameda S, Haefele SM, Hailu K *et al* (2021) The nutritional quality of cereals varies geospatially in Ethiopia and Malawi. *Nature* 594: 71–76

Hanikenne M, Talke IN, Haydon MJ, Lanz C, Nolte A, Motte P, Kroymann J, Weigel D, Kramer U (2008) Evolution of metal hyperaccumulation required cis-regulatory changes and triplication of HMA4. *Nature* 453: 391–395

He Y, Yang Q, Yang J, Wang YF, Sun X, Wang S, Qi W, Ma Z, Song R (2021) shrunken4 is a mutant allele of ZmYSL2 that affects aleurone development and starch synthesis in maize. *Genetics* 218: iyab070

Huang Y, Wang H, Huang X, Wang Q, Wang J, An D, Li J, Wang W, Wu Y (2019) Maize VKS1 regulates mitosis and cytokinesis during early endosperm development. *Plant Cell* 31: 1238–1256

Hussain D, Haydon MJ, Wang Y, Wong E, Sherson SM, Young J, Camakaris J, Harper JF, Cobbett CS (2004) P-type ATPase heavy metal transporters with roles in essential zinc homeostasis in *Arabidopsis*. *Plant Cell* 16: 1327–1339

Jyung WH, Ehmann A (1975) Zinc nutrition and starch metabolism in *Phaseolus vulgaris* L. *Plant Physiol* 55: 414–420

Klatte M, Schuler M, Wirtz M, Fink-Straube C, Hell R, Bauer P (2009) The analysis of *Arabidopsis* Nicotianamine synthase mutants reveals functions for Nicotianamine in seed iron loading and iron deficiency responses. *Plant Physiol* 150: 257–271

Lahner B, Gong J, Mahmoudian M, Smith EL, Abid KB, Rogers EE, Guerinot ML, Harper JF, Ward JM, McIntyre L *et al* (2003) Genomic scale profiling of nutrient and trace elements in *Arabidopsis thaliana*. *Nat Biotechnol* 21: 1215–1221

Le Jean M, Schikora A, Mari S, Briat JF, Curie C (2005) A loss-of-function mutation in AtYSL1 reveals its role in iron and nicotianamine seed loading. *Plant J* 44: 769–782

Li C, Liu C, Qi X, Wu Y, Fei X, Mao L, Cheng B, Li X, Xie C (2017) RNA-guided Cas9 as an *in vivo* desired-target mutator in maize. *Plant Biotechnol J* 15: 1566–1576

Liu H, Shi J, Sun C, Gong H, Fan X, Qiu F, Huang X, Feng Q, Zheng X, Yuan N *et al* (2016) Gene duplication confers enhanced expression of 27-kDa gamma-zein for endosperm modification in quality protein maize. *Proc Natl Acad Sci USA* 113: 4964–4969

Liu HJ, Jian L, Xu J, Zhang Q, Zhang M, Jin M, Peng Y, Yan J, Han B, Liu J *et al* (2020a) High-throughput CRISPR/Cas9 mutagenesis streamlines trait gene identification in maize. *Plant Cell* 32: 1397–1413

Liu HJ, Wang X, Xiao Y, Luo J, Qiao F, Yang W, Zhang R, Meng Y, Sun J, Yan S *et al* (2020b) CUBIC: an atlas of genetic architecture promises directed maize improvement. *Genome Biol* 21: 20

Long JK, Banziger M, Smith ME (2004) Diallel analysis of grain iron and zinc density in southern African-adapted maize inbreds. *Crop Sci* 44: 2019–2026

Maqbool MA, Beshir A (2019) Zinc biofortification of maize (*Zea mays* L.): status and challenges. *Plant Breeding* 138: 1–28

Nishiyama R, Kato M, Nagata S, Yanagisawa S, Yoneyama T (2012) Identification of Zn-Nicotianamine and Fe-2'-Deoxymugineic acid in the

phloem sap from Rice plants (*Oryza sativa* L.). *Plant Cell Physiol* 53: 381–390

Olsen LI, Hansen TH, Larue C, Osterberg JT, Hoffmann RD, Liesche J, Kramer U, Surble S, Cadarsi S, Samson VA *et al* (2016) Mother-plant-mediated pumping of zinc into the developing seed. *Nat Plants* 2: 16036

Robinson NJ, Procter CM, Connolly EL, Guerinot ML (1999) A ferric-chelate reductase for iron uptake from soils. *Nature* 397: 694–697

Simic D, Drinic SM, Zdunic Z, Jambrovic A, Ledencan T, Brkic J, Brkic A, Brkic I (2012) Quantitative trait loci for biofortification traits in maize grain. *J Hered* 103: 47–54

Tauris B, Borg S, Gregersen PL, Holm PB (2009) A roadmap for zinc trafficking in the developing barley grain based on laser capture microdissection and gene expression profiling. *J Exp Bot* 60: 1333–1347

Vert G, Grotz N, Dedaldechamp F, Gaymard F, Guerinot ML, Briat JF, Curie C (2002) IRT1, an *Arabidopsis* transporter essential for iron uptake from the soil and for plant growth. *Plant Cell* 14: 1223–1233

Wang J, Ji C, Li Q, Zhou Y, Wu Y (2018) Genome-wide analysis of the plant-specific PLATZ proteins in maize and identification of their general role in interaction with RNA polymerase III complex. *BMC Plant Biol* 18: 221

Waters BM, Grusak MA (2008) Whole-plant mineral partitioning throughout the life cycle in Arabidopsis thaliana ecotypes Columbia, *Landsberg erecta*, Cape Verde Islands, and the mutant line ysl1ysl3. *New Phytol* 177: 389–405

White PJ, Broadley MR (2009) Biofortification of crops with seven mineral elements often lacking in human diets – Iron, zinc, copper, calcium, magnesium, selenium and iodine. *New Phytol* 182: 49–84

von Wiren N, Klair S, Bansal S, Briat JF, Khodr H, Shioiri T, Leigh RA, Hider RC (1999) Nicotianamine chelates both Fe-III and Fe-II. Implications for metal transport in plants. *Plant Physiol* 119: 1107–1114

Wu FH, Shen SC, Lee LY, Lee SH, Chan MT, Lin CS (2009) Tape-Arabidopsis Sandwich – a simpler *Arabidopsis* protoplast isolation method. *Plant Methods* 5: 16

Zang J, Huo Y, Liu J, Zhang H, Liu J, Chen H (2020) Maize YSL2 is required for iron distribution and development in kernels. *J Exp Bot* 71: 5896–5910

Zhan J, Thakare D, Ma C, Lloyd A, Nixon NM, Arakaki AM, Burnett WJ, Logan KO, Wang D, Wang X *et al* (2015) RNA sequencing of laser-capture microdissected compartments of the maize kernel identifies regulatory modules associated with endosperm cell differentiation. *Plant Cell* 27: 513–531

Zhang Z, Yang J, Wu Y (2015) Transcriptional regulation of Zein gene expression in maize through the additive and synergistic action of opaque2, Prolamine-box binding factor, and O2 heterodimerizing proteins. *Plant Cell* 27: 1162–1172